Journal of Advances in Modeling Earth Systems

RESEARCH ARTICLE
10.1029/2018MS001381

Key Points:
- ISOLESC provides a quantitative framework for utilizing vapor-phase isotopic measurements to study local hydrological processes
- ISOLESC successfully reproduces ABL statistics, the time evolution of ABL vapor isotopic composition
- We quantified the sensitivity of ABL properties to mesh size and isotopic parameterizations

Correspondence to:
Z. Wei and X. Lee,
zhongwang.wei@hydra.t.u-tokyo.ac.jp;
xuhui.lee@yale.edu

Citation:
Wei, Z., Lee, X., & Patton, E. G. (2018). ISOLESC: A coupled isotope-LSM-LES-cloud modeling system to investigate the water budget in the atmospheric boundary layer. *Journal of Advances in Modeling Earth Systems*, *10*, 2589–2617. https://doi.org/10.1029/2018MS001381

Received 20 MAY 2018
Accepted 11 OCT 2018
Accepted article online 15 OCT 2018
Published online 29 OCT 2018
Corrected 15 JUL 2019

This article was corrected on 15 JUL 2019. See the end of the full text for details.

ISOLESC: A Coupled Isotope-LSM-LES-Cloud Modeling System to Investigate the Water Budget in the Atmospheric Boundary Layer

Zhongwang Wei[1,2], Xuhui Lee[1,2], and Edward G. Patton[3]

[1]School of Forestry and Environmental Studies, Yale University, New Haven, CT, USA, [2]Yale-NUIST Center on Atmospheric Environment, Nanjing University of Information Science and Technology, Nanjing, China, [3]National Center for Atmospheric Research, Boulder, CO, USA

Abstract Stable isotopes of water (H_2O, HDO, and $H_2{}^{18}O$) are tracers that provide powerful constraints on water transport processes in the atmosphere. This paper presents a description of an atmospheric boundary layer (ABL) simulation system called ISOLESC that couples water isotope fractionation processes with a land surface model, a large eddy simulation model, and a two-moment cloud microphysics parameterization. Results from two model configurations—one with shallow precipitating cumulus and the other for a cloud-free ABL—are presented to evaluate the model performance and determine its sensitivity to isotopic parameterizations. The coupled model successfully reproduces important ABL statistics (ABL height, cloud fraction, and cloud liquid water content), the expected effects of mixing and fractionation on the time evolution of ABL vapor isotopic composition, and observed diurnal variations of near-surface water vapor isotopic composition. For the current configuration, nondiscriminating entrainment contributes 17% to the subdaily time variation of near-surface vapor deuterium excess, while surface evapotranspiration contributes 83%. The isotopic compositions of water vapor and cloud water are insensitive to mesh resolution, but the profiles of cloud water specific humidity, rainwater specific humidity, and its isotopic ratios show moderate response to changes in grid size. Since ISOLESC resolves the energy containing scales of turbulent motions in the ABL and incorporates microphysical processes, it can be used for constraining ABL parameterizations. We find that a further improvement of raindrop reevaporation in the current cloud microphysical scheme is required in order to produce realistic near-surface raindrop deuterium excess for the case simulated here. We suggest that ISOLESC provides a quantitative framework for utilizing vapor-phase isotopic measurements to study local hydrological processes.

1. Introduction

Water in the atmospheric boundary layer (ABL) plays a crucial role in hydrological and climatic processes. By some estimates, most of the atmospheric vapor resides in this layer (Eltahir & Bras, 1996). Therefore, a strong water vapor specific humidity gradient typically forms at the interface between the ABL and the overlying free atmosphere. Boundary layer turbulence and entrainment lead to mixing of boundary layer and free-tropospheric air. Clouds forming at the top of the ABL transfer water from the ABL into the overlying free troposphere. Entrainment or turbulent diffusion driven by the water vapor specific humidity gradient can also transport water vapor to the free atmosphere. While both these processes dry the ABL, new vapor enters the ABL via evapotranspiration (ET) and advection of moisture from remote source regions. Water transport is an important heat redistributor, globally returning 82% of the surface net radiation energy to the atmosphere (Trenberth et al., 2009). ET and cloud condensation accomplish this energy redistribution, with the former removing heat from the Earth's surface and the latter depositing the heat above the ABL. Understanding the processes by which the ABL exchanges water with the land and the free atmosphere is at the heart of studies on land-atmosphere interactions.

Because phase changes for different water isotope species occur at slightly different rates, the isotopic compositions of ABL water have been used to advance our understanding of the linkages between land surface exchange and water vapor in the atmosphere (e.g., Gat, 2000). Evaporation favors the lighter water ($H_2{}^{16}O$) over the heavier isotopes (with deuterium in HDO and with heavy oxygen in $H_2{}^{18}O$), resulting in depletion in the vapor phase and enrichment in the condensed phase of the heavier isotopes (e.g., Jouzel et al.,

2013). On the other hand, condensation favors the heavier isotopes (Craig & Gordon, 1965). In ecosystems, the isotopic behavior of transpiration can be greatly affected by changes in humidity and subsequently the leaf-level energy balance. Two fractionation mechanisms occur during these phase changes. Equilibrium fractionation results from the lower saturation vapor pressures of HDO and $H_2{}^{18}O$ than that of H_2O, and kinetic fractionation results from the fact that HDO and $H_2{}^{18}O$ diffuse less efficiently in unsaturated air than does H_2O. Equilibrium fractionation occurs at the interface between cloud droplets and saturated air in the cloud layer, while both equilibrium fractionation and kinetic fractionation occur as liquid water on land evaporates (e.g., Aemisegger et al., 2014; Delattre et al., 2015) or when raindrops evaporate as they fall through the unsaturated air below the cloud layer (Bony et al., 2008).

The isotopic composition of water vapor in the ABL over land represents a composite signal of multiple influences, including air mass advection, moist convection, raindrop evaporation, surface ET, and entrainment of free-tropospheric air into the ABL through boundary layer growth. Synoptic weather events determine air mass evolution. The isotopic compositions of water arriving at a local ABL domain are influenced by the initial isotopic compositions at the moisture source (e.g., Risi et al., 2013) and modified by condensation/precipitation processes and surface ET along the air mass trajectory (e.g., Sodemann et al., 2008). According to the pseudo-adiabatic Rayleigh model, local moist convection that forms clouds and precipitation depletes the vapor in the boundary layer of ^{18}O and D (Noone, 2012; Smith, 1992). In precipitation events, raindrop evaporation can bring vapor in the near-surface atmospheric layers to the equilibrium state during sustained rain events (e.g., Lee et al., 2006), but the kinetic effect may force those layers to deviate from the equilibrium state if the surface air is not saturated (e.g., Wen et al., 2010). Water vapor evaporated from the land surface typically modifies the ^{18}O and D compositions of ABL water vapor, with the amplitude of the change depending largely on (1) the relative magnitude of soil evaporation to the total ET flux (Riley et al., 2003; Wong et al., 2017) and (2) the non–steady state nature of plant transpiration (Aemisegger et al., 2014; Lai & Ehleringer, 2011). Entrainment mixes free atmospheric vapor into the ABL, thus modifying the ABL vapor isotope compositions (Lee et al., 2011; Welp et al., 2012). The importance of these last two processes (ET and entrainment) varies strongly with the diurnal cycle of the ABL.

To the best of our knowledge, no currently available model allows for the explicit investigation of the subgrid-scale isotopic processes such as atmospheric shallow convection and isotopic non–steady state transpiration. The way to account for the interplay between the many processes affecting the atmospheric water cycle at the same time is to develop a new model with careful treatment of land surface processes for water isotopes and treatment of isotopes in cloud microphysics. In this paper, we describe a new modeling system that couples water isotope fractionation processes with a land surface model (LSM), a large eddy simulation (LES) model, and cloud microphysics parameterizations. This modeling system, abbreviated as ISOLESC, represents an expanded version of our previous isotopic LES model (ISOLES; Lee et al., 2011). Two important improvements are made. First, as ISOLES focuses primarily on enrichment of $C^{16}O^{18}O$ in plant leaves, its land surface modeling scheme is very primitive: It assumes that ET is contributed solely by plant transpiration (T) and that T is in isotopic steady state. In comparison, ISOLESC uses a more realistic LSM that considers both T and soil evaporation (E) and that the isotopic compositions of T and E are parameterized for non–steady state behaviors. Second, ISOLES can only be used for cloud-free boundary layers. In ISOLESC, cloud microphysics and isotopic fractionation mechanisms are explicitly parameterized and are fully coupled to the dynamics of the ABL flow. The main objectives of this study are (1) to examine the performance of the ISOLESC model in simulating standard ABL statistics and isotope fractionation processes, (2) to evaluate the impacts of model grid resolution and rain evaporation parameterization on vapor and liquid isotopic compositions, and (3) to quantify the relative contributions of entrainment, raindrop evaporation, and surface ET to changes in the ABL vapor isotopic compositions.

This study is motivated in part by the recent rapid increase of isotopic measurements of the vapor phase, thanks to advances in high-frequency laser spectrometry (Bailey et al., 2013; Griffis, 2013; Soderberg et al., 2012). Laser analyzers are portable, measure the vapor isotopic compositions continuously and at high temporal resolutions (seconds to minutes), and achieve accuracies comparable to that of the traditional mass spectrometry. Despite the explosive growth of laser-based measurements, our ability to interpret water transport processes with these measurements remains descriptive. A cloud-permitting turbulence-resolving isotopic ABL model may therefore provide a quantitative framework for interpreting these vapor-phase measurements to study hydrological processes. It is noted that this paper examines the isotopologues of

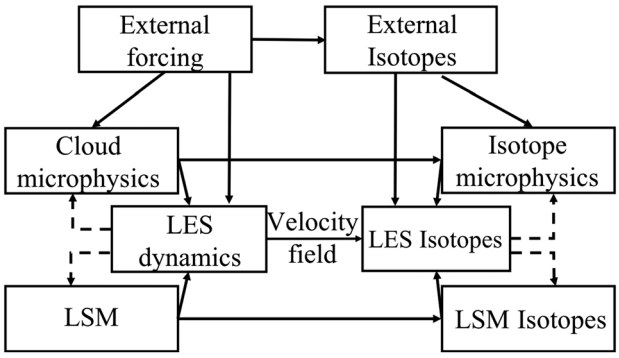

Figure 1. A box diagram showing the structure of the coupled Isotope-LSM-LES-Cloud modeling system (ISOLESC). Solid lines indicate that coupling occurs at the same time step, and dashed lines indicate that input variables are used in the next time step of integration. LES = large eddy simulation; LSM = land surface model.

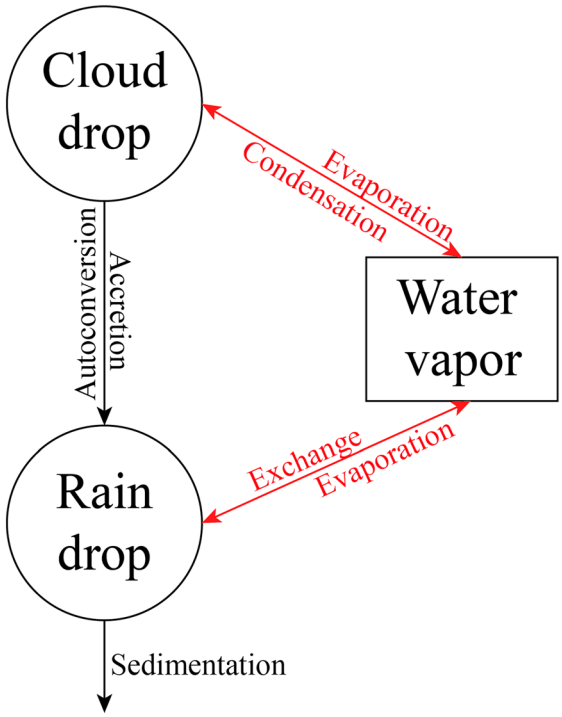

Figure 2. Depiction of cloud microphysical processes accounted for in ISOLESC. The solid red arrows represent isotopic fractionation during phase change. ISOLESC = a coupled Isotope-LSM-LES-Cloud modeling system.

water, with the term *isotopologue* meaning a molecule that contains an isotope, and the term will simply be referred to as *water isotope*.

2. Model Introduction

2.1. Overall Model Structure

Figure 1 shows a box diagram of the structure of the ISOLESC model system, which consists of six submodels: (1) LES Dynamics, (2) Cloud Microphysics, (3) LES Tracers, (4) Cloud Tracers, (5) LSM, and (6) LSM Tracers. The model system divides total atmospheric water into three pools: (1) water vapor, (2) cloud droplets, and (3) raindrops (Figure 2). Frozen hydrometeors are not currently allowed. The notations used in this study can be found in Table A1.

LES Dynamics resolves the turbulent motion using the surface heat and water vapor fluxes calculated by LSM as the lower flux boundary conditions and exchanges between the three water pools calculated by Cloud Microphysics as its source terms. At every integration time step, three humidity variables (water vapor, cloud water, and rainwater specific humidity) are diagnosed from three prognostic variables (liquid water potential temperature, total water specific humidity, and a variable containing the combination of water vapor specific humidity plus cloud water specific humidity) predicted by LES Dynamics during the previous time step.

LES Tracers predicts the transport and evolution of the water isotope species in water vapor and total and liquid water, and the subfilter-scale (SFS) fluxes of these species. At subfilter scales water isotopes are assumed to mix similarly, which therefore assumes that SFS mixing of water isotopes is nonfractionating. Cloud Tracers handles the fractionation during isotopic exchanges between the three water pools. The surface fluxes of the isotope species calculated by LSM Tracers provide the lower boundary conditions for LES Tracers.

LSM predicts the surface sensible and latent heat flux at every time step of integration. The primary input variables for LSM are provided by LES Dynamics at the first model grid point above the surface. Incoming solar and longwave radiation are also inputs to LSM and are updated each time step based on solar zenith angle and the liquid water path (LWP) from Cloud Dynamics.

LSM Tracers is the isotope equivalent of LSM and predicts the surface fluxes of the minor isotope species as the lower boundary condition for LES Tracers. It accounts for the fractionation processes in soil evaporation and plant transpiration and uses variables calculated by LES Dynamics and LSM as inputs.

Except LES Dynamics, all other model components can be individually turned on/off. This feature allows us to investigate the impacts of different atmospheric processes on variation of isotopic compositions of atmospheric water.

2.2. LES Dynamics

The National Center for Atmospheric Research's LES code has been described in a variety of earlier manuscripts (e.g., Moeng, 1984; Moeng & Wyngaard, 1988; Sullivan et al., 1996; Sullivan & Patton, 2011, 2012). The current model is based on the developments and extensions described in Moeng (2000), Patton et al. (2005, 2016), Vilà-Guerau de Arellano et al. (2005), and Lohou and Patton (2014).

2.2.1. Momentum Equations

The model integrates the equations for an ABL under the Boussinesq approximation (which also implies an assumption of hydrostatic balance) on a discretized three-dimensional grid, representing $\mathbf{u} = (u, v, w)$ in the streamwise x, spanwise y, and vertical z directions. A discrete Poisson equation for pressure π enforces incompressibility, and an equation for SFS turbulent kinetic energy e permits estimation of the influence of unresolved motions/processes.

The governing equations can therefore be expressed as

$$\frac{\partial \overline{\mathbf{u}}}{\partial t} + \overline{\mathbf{u}}\cdot\nabla\overline{\mathbf{u}} = -\nabla\boldsymbol{T} - f\widehat{k}\times\left(\overline{\mathbf{u}} - U_g\right) - \nabla\overline{\pi} + \widehat{k}\beta\left(\overline{\theta}_v - \theta_{v_0}\right) \tag{1}$$

$$\frac{\partial e}{\partial t} + \overline{\mathbf{u}}\cdot\nabla e = \mathrm{P} + \mathrm{B} + \mathrm{D} + \mathrm{E} \tag{2}$$

$$\overline{\mathbf{u}}\cdot\nabla = 0 \;\Rightarrow\; \nabla^2\overline{\pi} = r \tag{3}$$

In equations (1)–(3), f is the Coriolis parameter, $\widehat{k}$ is the unit vector in the vertical direction z, U_g is the geostrophic wind with horizontal (x, y) components (U_g, V_g), $\beta = g/\theta_{v_0}$ is the buoyancy parameter, $g$is the Earth's gravitational acceleration, and θ_{v_0} is a reference virtual potential temperature. The overbar $\overline{\ }$ represents the combined explicit horizontal and implicit vertical filter separating variables into their resolved and SFS components. The SFS momentum (T) fluxes and energy (e) are

$$T = \overline{u_I u_J} - \overline{u_I}\,\overline{u_J} \tag{4}$$

$$e = \frac{1}{2}\left(\overline{u_I u_I} - \overline{u_I}\,\overline{u_I}\right) \tag{5}$$

In equation (2), P and B represent SFS shear and buoyancy production, respectively, D represents SFS diffusion, and $\mathscr{E}$ represents dissipation. Equation (3) is formed by applying the discrete divergence operator to equation (1) and collecting all terms except the pressure in the source term r (Sullivan et al., 1996). At the upper boundary, Dirichlet conditions are imposed for w and e and Neumann conditions are imposed for all other variables; a sponge layer whose amplitude is controlled by the Brunt-Väisälä frequency at the upper boundary is imposed in the upper 20% of the domain to damp fluctuations for all variables. Lateral boundary conditions are periodic for all quantities. Second-order finite differences are used for vertical derivatives, and a pseudospectral method is used to calculate horizontal derivatives, where the top one-third wavenumbers are eliminated to avoid aliasing errors. Readers are referred to Sullivan et al. (1996), Sullivan and Patton (2011, 2012), and Patton et al. (2016) for further details. For computational efficiency, the National Center for Atmospheric Research (NCAR) LES currently updates the microphysics once per full Runge-Kutta time step. See Sullivan and Patton (2011, 2012) for further details.

2.2.2. Moist Thermodynamic Equations

To incorporate the influence of moist thermodynamics, the LES also includes conservation equations for liquid water potential temperature θ_l, total water specific humidity q_t, a humidity variable q_e comprising the sum of water vapor specific humidity q_v and cloud water specific humidity q_c (i.e., $q_e = q_v + q_c$), the number concentration of cloud droplets N_c, and the number concentration of raindrops N_r. These conservation equations are written as

$$\frac{\partial \overline{\theta_l}}{\partial t} + \overline{\mathbf{u}}\cdot\nabla\overline{\theta_l} = -\nabla\cdot\mathbf{B} + M_{\theta_l} \tag{6}$$

$$\frac{\partial \overline{q_t}}{\partial t} + \overline{\mathbf{u}}\cdot\nabla\overline{q_t} = -\nabla\cdot\mathbf{Q}_{q_t} + M_{q_t} \tag{7}$$

$$\frac{\partial \overline{q_e}}{\partial t} + \overline{\mathbf{u}}\cdot\nabla\overline{q_e} = -\nabla\cdot\mathbf{Q}_{q_e} + M_{q_e} \tag{8}$$

$$\frac{\partial \overline{N_c}}{\partial t} + \overline{\mathbf{u}}\cdot\nabla\overline{N_c} = -\nabla\cdot\mathbf{N}_{N_c} + M_{N_c} \tag{9}$$

$$\frac{\partial \overline{N_r}}{\partial t} + \overline{\mathbf{u}}\cdot\nabla\overline{N_r} = -\nabla\cdot\mathbf{N}_{N_r} + M_{N_r} \tag{10}$$

Symbols **B**, **Q**, and **N** denote SFS fluxes of temperature, specific humidity, and cloud/rain droplets, respectively, and M denotes the microphysical source and sink terms, which are discussed in section 2.3. Equations (6), (9), and (10) are new compared to previous versions of NCAR's cloudy LES (e.g., Lohou & Patton, 2014; Moeng, 1998, 2000).

From the three prognostic moist thermodynamic variables (θ_l, q_t, and q_e), three diagnostic humidity variables (water vapor specific humidity q_v, cloud liquid water specific humidity q_c, and rainwater specific humidity q_r) are reconstructed using the following diagnostic relationships:

$$q_v = \mathrm{MIN}(q_s, q_e) \tag{11}$$

$$q_c = \mathrm{MAX}(0, q_e - q_s) \tag{12}$$

$$q_r = q_t - q_e \tag{13}$$

where q_s is the saturation specific humidity and the MIN and MAX statements imply that the result is the minimum or maximum value of the two quantities in the parentheses. These diagnostic specific humidity variables are used as inputs to the cloud microphysical module described in section 2.3. To calculate q_s, one needs to know the local absolute temperature T that is calculated assuming hydrostatic equilibrium, the ideal gas law, and the first law of thermodynamics.

As introduced above, the NCAR LES predicts two specific humidity variables (q_t andq_e) and two number concentration variables (N_c and N_r). Integrating conservation equations for q_t and q_e as presented in equations (7) and (8) is advantageous since they vary smoothly across cloud and rain shaft boundaries, thereby reducing errors that would arise if one were to take derivatives of q_c and q_r independently. Predicting the cloud- and rain-droplet number concentrations increases the degrees of freedom associated with the hydrometeor spectra in the two moment bulk schemes, which improves representation of microphysical processes (such as adiabatic growth, collision-coalescence, raindrop evaporation, and sedimentation) and radiative transfer (Morrison et al., 2005). Additional information can be found in Morrison and Grabowski (2007).

Following Betts (1973), Wexler (1976), Emanuel (1994), and many others that followed, the NCAR LES uses the simplifying and close approximation to the first law of thermodynamics to write the liquid water potential temperature θ_l as

$$\theta_l \approx \theta - \frac{L}{C_p \Pi} q_c \tag{14}$$

where θ is the potential temperature, and Π is the Exner function:

$$\Pi = \left(\frac{p}{p_0}\right)^{\frac{R_{\mathrm{dry}}}{C_p}} = \frac{T}{\theta} \tag{15}$$

which can be viewed as a nondimensional pressure. Here R_{dry} and C_p are the specific gas constants for dry air and heat capacity, respectively. In equation (15), p_0 is a standard reference pressure that is usually taken as 1×10^5 Pa. A time-invariant hydrostatic mean pressure (p) profile is diagnosed by combining the equation of state, the Exner function, and an initial temperature profile. Liquid water potential temperature θ_l is conserved for reversible processes. Precipitation (rain, q_r) is an irreversible process due to evaporation in nonequilibrium (i.e., subsaturated) conditions and fallout at the surface. Therefore, equation (14) only includes the influence of condensed cloud water q_c. Rain's influence on θ_l enters through the microphysical source/sink terms affecting cloud water (q_c) and absolute temperature (T). Even though nonequilibrium processes through supersaturated or subsaturated exchange of cloud liquid and vapor are permitted by the microphysics, the supersaturation or subsaturation is likely quite small. Therefore, it is reasonable to neglect their nonequilibrium effects.

The NCAR LES typically relies on Deardorff's (1980) 1.5-order closure method to model the influence of SFS motions on the transport of momentum, heat, and all other scalars. Deardorff's (1980) 1.5-order closure follows an equation to estimate the energy contained in these unresolved motions (equation (2)) toward

calculating a spatially and temporally varying mixing efficiency associated with these motions. Thus, the quantities T, $\mathbf{B}$, $\mathbf{Q}_{q_e}$, $\mathbf{Q}_{q_t}$,$\mathbf{N}_{N_c}$, and $\mathbf{N}_{N_r}$ are modeled using

$$T = -\upsilon_M\left(\frac{\partial u_i}{\partial x_j} + \frac{\partial u_j}{\partial x_i}\right) \tag{16}$$

$$\mathbf{B} = -\upsilon_H\frac{\partial \theta_l}{\partial x_i} \tag{17}$$

$$\mathbf{Q}_{q_e} = -\upsilon_Q\frac{\partial q_e}{\partial x_i} \tag{18}$$

$$\mathbf{Q}_{q_t} = -\upsilon_Q\frac{\partial q_t}{\partial x_i} \tag{19}$$

$$\mathbf{N}_{N_c} = -\upsilon_N\frac{\partial N_c}{\partial x_i} \tag{20}$$

$$\mathbf{N}_r = -\upsilon_N\frac{\partial N_r}{\partial x_i} \tag{21}$$

It is currently assumed that heat, scalars, and number concentrations mix similarly; that is, $\upsilon_H = \upsilon_Q = \upsilon_N$ and that the turbulent eddy viscosity υ_M (and diffusivity υ_H) describing the transport of momentum (heat and scalars) by SFS motions are

$$\upsilon_M = c_m l e^{1/2} \tag{22}$$

$$\upsilon_H = c_h l e^{1/2} \tag{23}$$

where c_m is 0.1 (Moeng & Wyngaard, 1988) and c_h is

$$c_h = \left(1 + 2\frac{l}{\Delta}\right)c_m \tag{24}$$

which for neutral to unstable conditions implies that the Prandtl number for SFS motions is assumed equal to a value of 3. Variable l is a stability-dependent mixing length defined as

$$l = \text{MIN}\left(\Delta, c_N\frac{e^{1/2}}{N}\right) \tag{25}$$

Here Δ refers to the filter scale in the model, accounting for the explicit dealiasing of highest one-third wavenumbers associated with the pseudospectral differencing method used in the horizontal (x, y) directions:

$$\Delta = \left[\left(\frac{3}{2}\Delta_x\right)\left(\frac{3}{2}\Delta_y\right)\Delta_z\right]^{1/3} \tag{26}$$

In equation (25), c_N is a constant equal to 0.76 (Deardorff, 1980), and N_b is a Brunt-Väisälä frequency defined as

$$N_b = \left(\frac{g}{\theta_{v_0}}\frac{\partial \theta_v}{\partial z}\right)^{1/2} \tag{27}$$

where θ_v is the virtual potential temperature of cloudy air calculated assuming the following equation of state:

$$\theta_v = \theta\left[1 + \left(\frac{R_{\text{vap}}}{R_{\text{dry}}} - 1\right)q_v\right](1 - q_l) \tag{28}$$

where R_{vap} is the specific gas constant for water vapor.

Following Sommeria and Deardorff (1977), Deardorff (1980), and Cuijpers and Duynkerke (1993), buoyant production/destruction of SFS energy (term B in equation (2)) is expressed as

$$\mathrm{B} = \frac{g}{\theta_{v_0}}\left(a\mathbf{B} + b\mathbf{Q}_{q_t}\right) \tag{29}$$

where the coefficients a and b depend on the local thermodynamic state (i.e., whether the grid cell is saturated or unsaturated). For the unsaturated (dry, $q_c = 0$) case

$$a = a_{\mathrm{dry}} = 1 + \left(\frac{R_{\mathrm{vap}}}{R_{\mathrm{dry}}} - 1\right) q_e \tag{30}$$

$$b = b_{\mathrm{dry}} = \left(\frac{R_{\mathrm{vap}}}{R_{\mathrm{dry}}} - 1\right)\theta \tag{31}$$

and for the saturated case (wet, $q_c > 0$):

$$a = a_{\mathrm{wet}} = \frac{1 - q_e + q_s \frac{R_{\mathrm{vap}}}{R_{\mathrm{dry}}}\left(1 + \frac{L_v}{R_{\mathrm{vap}}\, T}\right)}{1 + \frac{L_v^2}{C_p R_{\mathrm{vap}}\, T^2}\, q_s} \tag{32}$$

$$b = b_{\mathrm{wet}} = \left(a_{\mathrm{wet}} \frac{L_v}{C_p T} - 1\right)\theta \tag{33}$$

Recall that rain can exist ($q_r > 0$) in grid points that are not saturated ($q_c = 0$). It is important to note that the form of equations (30)–(33) is specific to our choice to follow an equation for liquid potential temperature (θ_l); equations (30)–(33) would differ if one were to instead follow an equation for equivalent potential temperature (θ_e). It is also important to note that we have assumed an all-or-nothing approach such that any individual grid box is assumed to be either saturated or unsaturated; there is no possibility for a grid box to be partially saturated (e.g., Sommeria & Deardorff, 1977). Since supersaturation is prognostic in the Morrison microphysics scheme (Morrison & Grabowski, 2007, 2008), it is anticipated that errors introduced by presuming all-or-nothing saturation at cloud interfaces should be minimal.

At the upper boundary, we impose Dirichlet conditions for vertical velocity w and SFS energy e such that $w = e = 0$. Neumann conditions are imposed for all other quantities, where $\partial u/\partial z = 0$ and $\partial v/\partial z = 0$. For scalar quantities, we calculate the current horizontally averaged scalar gradient between the uppermost two grid points within the domain and then impose that same gradient between the uppermost grid point and a virtual point outside the domain. So the scalar gradient across the upper boundary is time evolving.

2.3. Cloud Microphysics

The bulk two-moment warm-rain scheme originally described by Morrison et al. (2005) has been incorporated into the NCAR LES to represent SFS microphysical proceses. Figure 2 presents a schematic representation of the cloud microphysics in ISOLESC. The size distributions of the cloud droplets N_c and raindrops N_r are computed from the following gamma distribution function

$$N(D) = N_0 D_p{}^{\mu} e^{-\lambda D} \tag{34}$$

where D_p is particle diameter, andN_0, μ, and λ are the intercept, shape parameter, and slope parameter, respectively (Morrison et al., 2009). Here N_0 and λ are derived from specified μ, the LES-predicted total number concentration N, and specific humidity of each species following the Euler gamma function and an assumed power law mass-diameter relationship of the hydrometeors for each species (Morrison et al., 2005, 2009; Morrison & Grabowski, 2007). For cloud droplets, μ is derived from the theoretical formulation of Khvorostyanov and Curry (1999). For raindrops, μ is assumed equal to 0, meaning that raindrops follow a Marshal-Palmer (exponential) size distribution (Morrison et al., 2005). These size distributions are used to predict the mass mixing ratios. Cloud condensation nuclei spectra are derived using an assumed lognormal aerosol size distribution using specified parameters consistent with ammonium sulfate.

In equations (6)–(10), the *M*terms represent the microphysical source/sink terms for θ_l, N, and q; from Morrison et al. (2005, 2009) and Morrison and Grabowski (2008), they are written as

$$M_{\theta_l} = \left(\frac{\partial \theta_l}{\partial t}\right)_{\text{con/evap}} \tag{35}$$

$$M_{q_t} = \left(\frac{\partial q_t}{\partial t}\right)_{\text{act}} + \left(\frac{\partial q_t}{\partial t}\right)_{\text{evap}} + \left(\frac{\partial q_t}{\partial t}\right)_{\text{acc}} + \left(\frac{\partial q_t}{\partial t}\right)_{\text{auto}} + \left(\frac{\partial q_t}{\partial t}\right)_{\text{sed}} \tag{36}$$

$$M_{q_e} = \left(\frac{\partial q_e}{\partial t}\right)_{\text{act}} + \left(\frac{\partial q_e}{\partial t}\right)_{\text{evap}} + \left(\frac{\partial q_e}{\partial t}\right)_{\text{acc}} + \left(\frac{\partial q_e}{\partial t}\right)_{\text{auto}} + \left(\frac{\partial q_e}{\partial t}\right)_{\text{sed}} \tag{37}$$

$$M_{N_c} = \left(\frac{\partial N_c}{\partial t}\right)_{\text{act}} + \left(\frac{\partial N_c}{\partial t}\right)_{\text{evap}} + \left(\frac{\partial N_c}{\partial t}\right)_{\text{acc}} + \left(\frac{\partial N_c}{\partial t}\right)_{\text{auto}} + \left(\frac{\partial N_c}{\partial t}\right)_{\text{self}} + \left(\frac{\partial N_c}{\partial t}\right)_{\text{sed}} \tag{38}$$

$$M_{N_r} = \left(\frac{\partial N_r}{\partial t}\right)_{\text{act}} + \left(\frac{\partial N_r}{\partial t}\right)_{\text{evap}} + \left(\frac{\partial N_r}{\partial t}\right)_{\text{acc}} + \left(\frac{\partial N_r}{\partial t}\right)_{\text{auto}} + \left(\frac{\partial N_r}{\partial t}\right)_{\text{self}} + \left(\frac{\partial N_r}{\partial t}\right)_{\text{sed}} \tag{39}$$

where subscripts act, con, evap, aac, auto, self, and sed represent droplet activation of aerosols (for cloud water only), condensation, evaporation, accretion of cloud droplets by rain, autoconversion of cloud droplets to rain, self-collection of cloud water and rain, and sedimentation. The change in q_c resulting from activation is calculated by assuming that newly formed droplets have an initial radius of 1 μm. The parameterization describing cloud droplet activation applies the Kohler theory to a lognormal size distribution for aerosols (Morrison & Grabowski, 2007). Accretion of cloud droplets by rain assumes a simple gravitational collection kernel. The autoconversion tendencies ($\left(\frac{\partial q}{\partial t}\right)_{\text{auto}}$ and $\left(\frac{\partial N}{\partial t}\right)_{\text{auto}}$) follow Beheng (1994) to represent the transfer of N and q from the cloud droplet class to the rain droplet class due to growth by vapor diffusion and coalescence. The self-collection tendency of cloud droplets and rain $\left(\frac{\partial N}{\partial t}\right)_{\text{self}}$ also follows Beheng (1994). Rain sedimentation is treated diagnostically in a manner similar to Reisner et al. (1998). Note that direct condensation of vapor to rain is not allowed (but isotopic exchange occurs between rain and vapor, see section 2.6). The temperature tendency is parameterized by following Morrison and Grabowski (2007), which is given by

$$\left(\frac{\partial T}{\partial t}\right)_{\text{con/evap}} = \frac{L_v}{C_p} C \tag{40}$$

where C is the net condensation rate including both cloud and rain. With the updated temperature and specific humidities of vapor and cloud, the updated liquid water potential temperature can be computed using equation (14).

The raindrop evaporation tendency is given by Morrison et al. (2009):

$$\text{EPSR} = 2\pi N_{0r} \rho D_v \left[\frac{f_1}{\lambda_r^2} + f_2 \left(\frac{a_r \rho}{\mu_a}\right)^{\frac{1}{2}} S_c^{\frac{1}{3}} \frac{\Gamma(b_r/2 + 5/2)}{\lambda_r^{b_r/2+5/2}}\right] \tag{41}$$

$$\left(\frac{\partial q_r}{\partial t}\right)_{\text{evap}} = \text{EPSR} \frac{q_v - q_s}{AB} \tag{42}$$

where S is the liquid water saturation ratio, and N_{0r} and λ_r are derived from the predicted rain mixing ratio and number concentration (Morrison et al., 2005, 2009). For a given rain mixing ratio, evaporation rate depends on N_{0r} only (Morrison et al., 2009). In addition, D_v is the diffusivity of water vapor in air; f_1 and f_2 are ventilation parameters; A and B are thermodynamic parameters related to the release of latent heat; a_r and b_r are fall speed parameters for rain whereby the fall speed is a function of particle diameter D given by $a_r D^{b_r}$; μ_a is

the dynamic viscosity of air, S_c is the Schmidt number, and Γ is the Euler gamma function. If there is no cloud water/rainwater, the microphysical calculation is skipped.

2.4. Land Surface Model

The National Centers for Environmental Prediction/Oregon State University/Air Force/Office of Hydrology (NOAH) LSM, version 2.1 (Chang et al., 1999) provides the lower boundary conditions at every horizontal grid point in the LES. NOAH is widely adopted by the weather forecasting community (e.g., the Weather Research and Forecast model community) for investigation of the hydrologic coupling in the soil-water-vegetation system.

A surface energy balance equation constrains the total exchange of heat and moisture at the surface, where heat and moisture fluxes represent the sum of contributions from unresolved vegetation and from the soil. A *big-leaf* assumption determines the heat and moisture exchange from the unresolved canopy using a canopy resistance obtained by coupling photosynthesis with incident radiation. A simple linear function of soil moisture availability, fraction of vegetation cover, and potential ET determines the soil evaporation rate.

Patton et al. (2005) describe the coupling between NCAR's LES and the NOAH LSM (version 2.7.1; Mitchell, 2005). For the simulations discussed here, ground vegetation is a perennial grass with a leaf area index of 4 m^2/m^2, a roughness length of 0.1 m, and a surface albedo of 0.2. The LSM requires wind speed, air temperature, water vapor specific humidity, air pressure, incoming radiation (shortwave and longwave), LAI, canopy scattering, stomatal characteristics, leaf distribution, soil characteristics, and albedo as inputs. The default initial soil moisture and temperature profiles come from a 2-year the High-Resolution Land Data Assimilation System (HRLDAS) (Chen et al., 2007) simulation targeting the 26 June 1997, Southern Great Plains case simulated by Lohou and Patton (2014). Additional information can be found in Table A2. LES-derived horizontal wind speed, air temperature, specific humidity, air pressure, and incoming radiation (shortwave and longwave) at the first model level drive the LSM.

2.5. LES Isotopes

NCAR's LES can simulate the evolution and transport of an arbitrary number of passive tracers. These tracers are transported similarly as water vapor and heat, but their sources and sinks do not influence the wind field, the cloud microphysics, or other dynamical aspects of the flow. We take advantage of this capability to simulate the transport and diffusion of the minor isotopologues of water.

Because the isotope tracers ($HD^{16}O$ or $H_2{}^{18}O$) are related to specific humidity, the conserved isotopic variables will follow notation similar to specific humidity but denoted by subscript *i*. For example, q_{t_i} is defined as the ratio of the mass of the minor isotope molecules in the vapor and the liquid (cloud droplets and raindrops) to the mass of moist air. The conservation equations for the isotope specific humidity variables are written in a similar way to equations (7) and (8) as

$$\frac{\partial \overline{q_{t_i}}}{\partial t} + \overline{\mathbf{u}} \cdot \nabla \overline{q_{t_i}} = -\nabla \cdot \mathbf{Q}_{q_{t_i}} + M_{q_{t_i}} \tag{43}$$

$$\frac{\partial \overline{q_{e_i}}}{\partial t} + \overline{\mathbf{u}} \cdot \nabla \overline{q_{e_i}} = -\nabla \cdot \mathbf{Q}_{q_{e_i}} + M_{q_{e_i}} \tag{44}$$

In these equations, the **Q** terms are subfilter fluxes of the minor isotope species, and the *M* terms are their sources and sinks calculated by Cloud Tracers (section 2.6).

From the LES prognostic variables q_{t_i} and q_{e_i}, q_{c_i}, and q_{r_i} are diagnosed using

$$q_{c_i} = \frac{q_{e_i}}{1 + q_v / q_c \cdot \alpha_{v,l}} \tag{45}$$

$$q_{v_i} = q_{e_i} - q_{c_i} \tag{46}$$

$$q_{r_i} = q_{t_i} - q_{e_i} \tag{47}$$

where q_{c_i}, q_{v_i}, and q_{r_i} denote the isotopic specific humidity of cloud droplets, vapor, and raindrops, respectively, and $\alpha_{v,\,l}$ is the equilibrium fractionation factor at air temperature *T* (Majoube, 1971). In equation (45), cloud liquid water is assumed to be instantaneously in isotopic equilibrium with the vapor in the same

grid cell, as the equilibration time (2 s) for cloud droplets (Jouzel, 1986; J.-E. Lee et al., 2007; Lee & Fung, 2008) is shorter than the LES time step (~ 3 s). To ensure that the ISOLESC correctly produces isotopic variabilities in the boundary layer, we completed a test run and found that the isotopic mass budget was closed to within the numerical uncertainty ($< 10^{-14}$ kg/kg) in each grid cell during each transport time step.

2.6. Isotope Microphysics

The Isotope Microphysics module computes the source and sink terms for the isotope species associated with phase changes occurring both in-cloud and during the reevaporation of rainwater. Isotopic fractionation only occurs during phase changes and is parameterized based upon the instantaneous resolved-scale quantities.

In equations (43) and (44) the M terms are thus given as

$$M_{q_{t_i}} = \left(\frac{\partial q_{t_i}}{\partial t}\right)_{\text{act}} + \left(\frac{\partial q_{t_i}}{\partial t}\right)_{\text{evap}} + \left(\frac{\partial q_{t_i}}{\partial t}\right)_{\text{acc}} + \left(\frac{\partial q_{t_i}}{\partial t}\right)_{\text{auto}} + \left(\frac{\partial q_{t_i}}{\partial t}\right)_{\text{sed}} \tag{48}$$

$$M_{q_{e_i}} = \left(\frac{\partial q_{e_i}}{\partial t}\right)_{\text{act}} + \left(\frac{\partial q_{e_i}}{\partial t}\right)_{\text{evap}} + \left(\frac{\partial q_{e_i}}{\partial t}\right)_{\text{acc}} + \left(\frac{\partial q_{e_i}}{\partial t}\right)_{\text{auto}} + \left(\frac{\partial q_{e_i}}{\partial t}\right)_{\text{sed}} \tag{49}$$

Equations (48) and (49) allow us to calculate how the subgrid-scale phase changes modify air-droplet isotopic exchange during the raindrop descent below the cloud layer, and also in-cloud processing and conversions between vapor, cloud drops, and raindrops. The autoconversion, accretion, self-collection, and sedimentation processes modify the liquid water amount from the existing condensate, thus occurring with no fractionation. It is noted that as q_{t_i} and q_{e_i} combine different forms of water (vapor, cloud, and rain), they are unaffected by microphysical processes. In equations (36) and (48), the only remaining tendency is sedimentation, while equations (37) and (49) lose the activation tendency because it has already been accounted for by the transfer of water in the vapor to the cloud form.

Kinetic fractionation occurs when raindrops fall into the undersaturated layer beneath the cloud (Stewart, 1975). Although kinetic fractionation would normally cause the liquid at the air-droplet interface to become more enriched in HDO and $H_2{}^{18}O$ than the bulk liquid within the droplet, strong ventilation of the raindrops in natural conditions promotes rapid circulation within the liquid to the extent that the raindrops can be assumed to be of uniform isotopic compositions (Stewart, 1975; Yoshimura et al., 2008). The raindrop evaporation isotopic tendency is calculated in a consistent manner with the standard water microphysics (equations (41) and (42) but reflecting the isotopic diffusivity and the isotopic equivalent of vapor deficit under unsaturated condition, as

$$\text{EPSR}_i = 2\pi N_{0r}\rho D_{v_i}\left[\frac{f_1}{\lambda_r^2} + f_2\left(\frac{a_r\rho}{\mu_a}\right)^{\frac{1}{2}}\left(S_c\frac{D_{v_i}}{D_v}\right)^{\frac{1}{3}}\frac{\Gamma(b_r/2+5/2)}{\lambda_r^{b_r/2+5/2}}\right] \tag{50}$$

$$\left(\frac{\partial q_{r_i}}{\partial t}\right)_{\text{evap}} = \text{EPSR}_i \times \left[q_{v_i} - \frac{q_{r_i}}{q_r}\frac{1}{\alpha_{\text{liq}}}\left(q_s + \frac{q_v(AB-1)}{AB}\right)\right] \tag{51}$$

where D_{v_i} is diffusivity of HDO or $H_2{}^{18}O$ in air (Stewart, 1975). The last term in equation (51) can be derived from equation B19 of Blossey et al. (2010). This derivation assumes that their parameter β is zero and B19 is multiplied by the saturation vapor mixing ratio that is embedded in the factor C_r in their equation B19. Note that AB in here is equivalent to $1 + b_l$ in Blossey et al. (2010). For saturated conditions, following Blossey et al. (2010), equation (51) becomes

$$\left(\frac{\partial q_{r_i}}{\partial t}\right)_{\text{evap}} = \text{EPSR}_i \times \left[q_{v_i} - \frac{q_{r_i}}{q_r}\frac{1}{\alpha_{\text{liq}}}\right] \tag{52}$$

The above treatment of the rain-vapor isotopic exchange/evaporation (equations (50) and (51)) is consistent with the underlying microphysics, has no tunable parameters, and is the default in our model.

Kinetic fractionation creates large uncertainties for climate model simulations of rainwater isotope composition. One key uncertainty, especially in global climate models (GCMs), lies in estimating the effective relative humidity around evaporating raindrops (Bony et al., 2008; Stewart, 1975). Some modeling studies prescribe the subcloud layer with constant relative humidity, typically 95% (Schlesinger et al., 1988; Yoshimura et al., 2008), while other studies parameterize this humidity as a function of the resolved relative humidity (equation (56), section 2.6; Bony et al., 2008; Nusbaumer et al., 2017). For comparison, in an isotope-enabled GCM, the isotopic mass conservation is expressed as

$$m\frac{dR_r}{dm} = \beta(R_r - \gamma R_v) \tag{53}$$

where m is the mass of the raindrop, $R_r = q_{r_i}/q_r$ and $R_v = q_{v_i}/q_v$ are the ratios of the mass of the heavier isotope to the normal water for rain and vapor, respectively. Parameters γ and β are related to the equilibrium and kinetic fractionations as

$$\beta = \frac{1 - \alpha_e(D/D_i)^n(1 - \mathrm{RH}_e)}{\alpha_e(D/D_i)^n(1 - \mathrm{RH}_e)} \tag{54}$$

and

$$\gamma = \frac{\alpha_e \mathrm{RH}_e}{1 - \alpha_e(D/D_{v_i})^n(1 - \mathrm{RH}_e)} \tag{55}$$

where α_e is the equilibrium isotope fractionation factor, which is a function of temperature.D_{v_i} and D are the molecular diffusivities of isotopic vapor and normal vapor in ambient air, n = 0.58 is the degree of freedom (Gat, 2000), and RH_e is the effective relative humidity (Bony et al., 2008; Nusbaumer et al., 2017) defined by

$$\mathrm{RH}_e = 0.9 + 0.1\mathrm{RH}_{\mathrm{grid}} \tag{56}$$

where $\mathrm{RH}_{\mathrm{grid}}$ is the resolved relative humidity. Integrating equations 53–55, we have

$$\left(\frac{\partial q_{r_i}}{\partial t}\right)_{\mathrm{evap}} = \frac{q_{r_i0} - \left\{\varepsilon\left[\left(\frac{q_{r_i0}}{q_{r0}} - \gamma\frac{q_{v_i0}}{q_{v0}}\right)(m/m_0)^{\beta} + \gamma\frac{q_{v_i0}}{q_{v0}}\right] + (1-\varepsilon)\frac{q_{r_i0}}{q_{r0}}\right\}\cdot q_r}{\mathrm{d}t} \tag{57}$$

where subscript 0 indicates original values without accounting for raindrop evaporation, m denotes the mass of bulk ($H_2{}^{16}O$) rainwater in a grid cell, and ε, a tunable parameter representing the fraction of the rain droplets reaching the isotopic equilibrium state, is assumed to be 0.95 in this study (Hoffmann et al., 2000).

Isotopic exchange can be interpreted as a reversible Rayleigh distillation process, but such an approximation neglects isotopic exchange between rainwater and the surrounding vapor in cloudy air and diffusion-driven kinetic fractionation in the subsaturated air when rain falls outside of the clouds. In a reversible moist adiabatic process, where all exchange between vapor and condensate occurs at saturation, condensate is retained in the parcel and no precipitation occurs, and liquid condensate follows the Rayleigh distillation model. So we also use this Rayleigh model to approximate the isotopic tendency due to rain evaporation $\left(\frac{\partial q_{r_i}}{\partial t}\right)_{\mathrm{evap}}$ (see Noone, 2012, equation (13)), in which the nonequilibrium effect of evaporation in subsaturated conditions is neglected. A direct comparison of precipitation isotopic ratios from these three runs will determine how the varying formulations of isotopic fractionation affect the precipitation isotopic compositions.

2.7. LSM Isotopes

This module provides the lower boundary conditions for the LES tracer calculations. It historically expresses the isotopic compositions of soil evaporation, canopy transpiration, and ET in the delta notation, and here we convert the delta values to the actual mass flux of the minor isotopes. The delta value (δ) in the unit of ‰ is related to the mass ratio as

$$\delta_i = \left(\frac{R_i}{R_{\mathrm{Standard}}} - 1\right)\times 1{,}000 \tag{58}$$

where $R = q_i/q$ is the ratio of the $H_2{}^{18}O$ or HDO mass to the $H_2{}^{16}O$ mass and R_{standard} is the corresponding mass ratio of the Vienna Standard Mean Ocean Water.

The ET isotope ratios are given from transpiration (T_r) and evaporation (E) flux and their respective isotope signals:

$$\delta_{\mathrm{ET}} = \frac{\delta_E \mathrm{E} + \delta_T \mathrm{T}_r}{\mathrm{ET}} \tag{59}$$

The isotopic composition of soil evaporation (δ_E) is calculated with the Craig-Gordon model (Craig & Gordon, 1965):

$$\delta_E = \frac{\alpha_e \delta_L - \mathrm{RH}^* \delta_a - \varepsilon_e - (1 - \mathrm{RH}^*)\varepsilon_k}{1 - \mathrm{RH}^* + (1 - \mathrm{RH}^*)\varepsilon_k / 1,000} \tag{60}$$

where δ_a is the isotopic ratio of vapor obtained from LES Tracers at the first model grid height, δ_s is the isotopic ratio of soil water that is set to -10‰ and -70‰ for $\delta^{18}O$ and δD, respectively, and kept at these constant values over the course of the simulation, ε_k (28‰ for $\delta^{18}O$ and 25‰ for δD) is the isotopic kinetic fractionation associated with soil evaporation, RH^* is relative humidity in reference to the temperature of the soil, α_e is the equilibrium fractionation factor at the soil temperature, and $\varepsilon_e = 1 - \alpha_e$.

The δ of transpiration under non–steady state is given by

$$\delta_T = \delta_x + \frac{\delta_{L,e} - \delta_{L,es}}{\alpha_k \alpha_e (1 - \mathrm{RH}_c{}^*)} \tag{61}$$

where the δ of water at the evaporating site in the leaves in steady state ($\delta_{L,\,es}$) is calculated by inverting the Craig-Gordon model:

$$\delta_{L,es} = \delta_x + \varepsilon_e + \varepsilon_{\mathrm{ck}} + \mathrm{RH}_c{}^* (\delta_a - \varepsilon_k - \delta_x) \tag{62}$$

and $\delta_{L,\,e}$ is the delta value of the water at the evaporating site in the leaves in non–steady state. Here $\mathrm{RH}_c{}^*$ is relative humidity expressed as a fraction in reference to the canopy temperature. The canopy kinetic fractionation factor $\varepsilon_{\mathrm{ck}}$ is given by (Lee et al., 2009)

$$\varepsilon_{ck} = \frac{21 r_c + 19 r_b}{r_a + r_b + r_c} \tag{63}$$

where r_a, r_b, and r_c are the aerodynamic, the leaf boundary layer, and the canopy resistances, respectively. In equation (61), $\alpha_k = 1 + \varepsilon_{ck}/1,000$ is the fractionation factor for diffusion. The isotope ratio of xylem water δ_x is assumed equal to that of the soil water. By considering temporal changes in the water content and the Péclet effect (Farquhar & Cernusak, 2005), $\delta_{L,\,e}$ is given by

$$\delta_{L,e} = \delta_{L,es} - \frac{(1.0 + \varepsilon_k/1,000)\alpha_{\mathrm{eq}} r_t}{w_i} \frac{1 - e^{-P}}{P} \frac{d\left(W \times \left(\delta_{L,e} - \delta_x\right)\right)}{dt} \tag{64}$$

where W is the leaf water content, w_i is the mole fraction of water vapor in the intercellular space, P is the Péclet number (dimensionless), and r_t is the total resistance to the diffusion of water vapor. Here w_i is calculated from relative humidity. Constant values are used for W and P (Wei et al., 2018). Equation (64) is solved iteratively by finding a zero difference between its left- and right-hand side. Specific values can be found in Table A2.

The LSM Tracer module requires two sets of inputs. The first set of input variables, such as wind speed, air pressure, relative humidity, and water vapor isotope compositions, is provided by LES Dynamics and LES Tracers at the first model level above the surface. The second set of inputs (e.g., transpiration rate, canopy temperature, canopy, and soil resistance) comes from the standard LSM code.

Once the isotopic composition of ET flux is known, the surface flux of the minor isotopologue i is given by

$$\overline{w' q_{v_i}'} = \overline{w' q_v'} \left(\frac{\delta_{\mathrm{ET}}}{1,000} - 1 \right) R_{\mathrm{Standard}} \tag{65}$$

where $\overline{w' q_v'}$ is the ET flux computed by the LSM. Equation (65) is the surface flux boundary condition for LES Tracers.

Table 1
A Summary of LES Configurations Used in This Study

Run	Grid points	(Δ_x, Δ_y, Δ_z) (m)	Description		
			Underlying surface	Cloud	Isotope
A	128 × 128 × 100	(100, 100, 40)	Ocean[a]	Morrison scheme + advection	No
B	256 × 256 × 200	(25, 25, 20)	Land surface[b]	Morrison scheme	Yes
C	256 × 256 × 200	(25, 25, 20)	Land surface[b]	No cloud	Yes
D	256 × 256 × 200	(25, 25, 20)	Land surface[b]	No cloud	Yes, with $\delta_{ET} = \delta_v$
E	128 × 128 × 100	(50, 50, 40)	Land surface[b]	Morrison scheme	Yes
F	256 × 256 × 200	(25, 25, 20)	Land surface[b]	Morrison scheme	Yes, with RH_e used in rain reevaporation
G	256 × 256 × 200	(25, 25, 20)	Land surface[b]	Morrison scheme	Yes, with reverse Rayleigh distillation in rain reevaporation

Note. LES = large eddy simulation; ET = evapotranspiration.
[a]The underlying surface and advection are the same as in vanZanten et al. (2011). [b]The underlying surface is configured in the same way as in Patton et al. (2005).

2.8. External Forcing

Horizontal and/or vertical scalar advection can be added to the conservation equations of θ_l, q_t, and q_e as additional external forcing. Externally imposed geostrophic wind and solar forcing drive the model.

3. Model Runs

We present seven simulations designed to evaluate model performance for both standard ABL processes as well as isotopic parameterizations. Table 1 summarizes the parameterization schemes and grid resolutions used in these model runs. Except for Run A, all simulations started at 04:00 local time and the results are presented for hours after 06:00 to allow for an initial spin-up period of 2 hr.

For Run A, a 24-hr duration was chosen. Run A is designed to demonstrate the skill of the NCAR LES in simulating standard ABL features during the Rain in Cumulus over the Ocean (RICO) experiment (vanZanten et al., 2011) against simulation results produced by 12 different LES models. This is a case of cumulus cloud with precipitation, with the external forcing prescribed according to vanZanten et al. (2011). Run A does not use the NOAH LSM because the RICO case relies on an ocean surface flux parameterization using a bulk transfer coefficient method.

To ensure that the subsequent simulations produce rain, Runs B–G use the same RICO-derived initial atmospheric conditions as Run A. Runs B–G also (1) activate the LES Tracers module, (2) deactivate large-scale advection in order to prevent contamination by water sources of unknown isotopic compositions, and (3) calculate surface fluxes from a coupling between the LES and the NOAH LSM using the default configuration described in section 2.6.

Run B serves as a control run, utilizing 256 × 256 grid points in the horizontal directions and 200 grid points in the vertical direction using the default suite of cloud, land surface, and isotopic process parameterizations. Runs C and D are simulations of a cloud-free boundary layer in which the Cloud Microphysics module is turned off. These two runs investigate the influence of the isotopic parameterization of ET on the variability of water vapor isotopes in the ABL. In Run C, the isotopic compositions of the land ET are computed by the LSM Tracers module. In Run D, δ_{ET} is forced to be equal to the vapor isotopic composition δ_v, an arrangement that essentially turns off the impact of land ET on the boundary layer vapor isotopic compositions. Run E is a grid resolution sensitivity experiment; compared to Run B (resolution 25 × 25 × 20 m), this run has a relatively coarse resolution (128 × 128 × 100 grid points with grid resolution of 50 × 50 × 40 m).

Runs F and G are configured similar to Run B except that a different isotopic parameterization of raindrop reevaporation is used in each. Run B uses a local treatment of rain vapor isotopic exchange that is faithful to the standard water microphysics (equations 50–52). Here the rainwater relies only on local information and does not require tunable parameters. The only assumption made concerns the rain size distribution. Run F uses the effective relative humidity to account for the fact that the air surrounding the raindrop is more humid than the grid cell average (equation (56), Bony et al., 2008; Nusbaumer et al., 2017). In Run G, raindrop evaporation

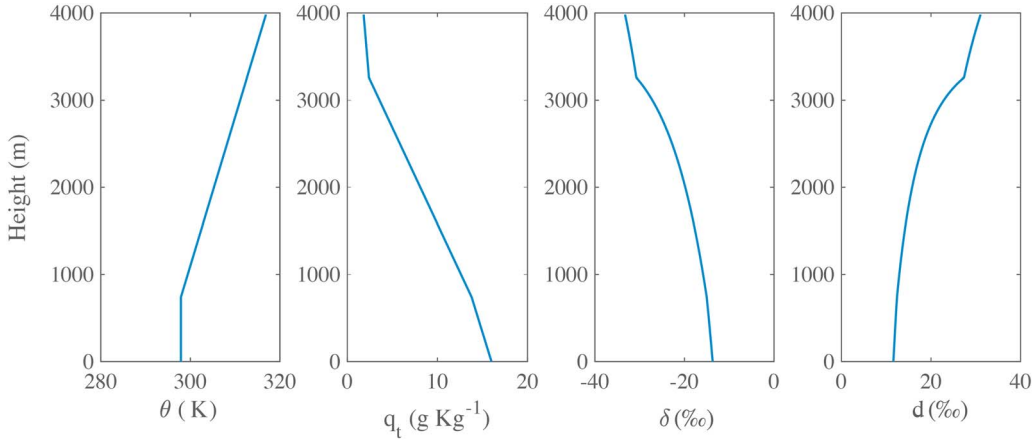

Figure 3. Initial profiles of potential temperature, specific humidity ($q_t = q_e = q_v$), water vapor δ (^{18}O), and vapor deuterium excess (d).

is assumed to follow the reversible Rayleigh distillation mechanism whereby the raindrops and the vapor are in isotopic equilibrium and no kinetic fractionation takes place.

The initial atmospheric profiles of horizontally averaged potential temperature and specific humidity for all simulations are presented in Figure 3. Initial horizontal winds are constructed as piecewise linear fits of averaged radiosonde profiles launched 2–6 times daily from Spanish Point (Barbuda) during RICO. The RICO case assumes that the imposed geostrophic winds are constant over the duration of the simulation. Detailed information can be found in vanZanten et al. (2011).

The initial profile of the vapor $\delta^{18}O$ is assumed to follow the Rayleigh distillation relationship (Lee et al., 2011):

$$\delta^{18}O = 8.99\ \ln(q_v/0.622) - 42.9 \tag{66}$$

where q_v is the initial radiosonde-derived horizontally averaged atmospheric water vapor specific humidity shown in Figure 3. The initial profile of the vapor deuterium excess (d), which is defined as $\delta D - 8\delta^{18}O$ is based on the mean profile from the observation of He and Smith (1999). The initial profile of the vapor δD is calculated as $d + 8\delta^{18}O$. These initial profiles are shown in Figure 3.

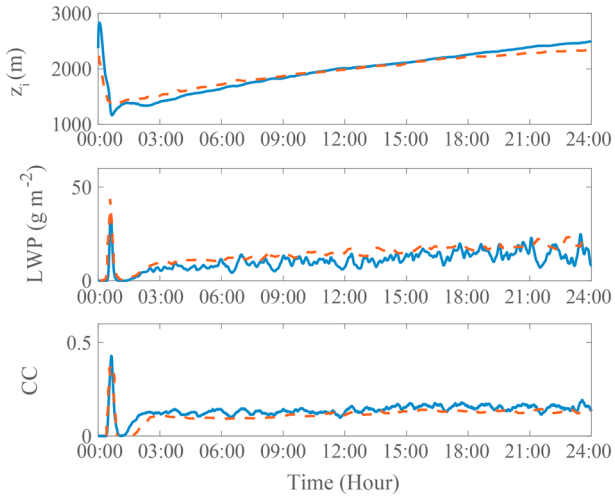

Figure 4. Time series of boundary layer height (z_i), liquid water path (LWP), and cloud cover (CC) fraction in Run A (solid blue lines). The red dashed lines depict time traces of ensemble-averaged results from 12 different LES codes from vanZanten et al. (2011). LES = large eddy simulation.

4. Performance Evaluation

4.1. Standard ABL Features

To evaluate our model's capability to simulate boundary layer dynamics, we compare our simulation with the ensemble average of 12 LESs shown in vanZanten et al. (2011; Run A, Table 1). The RICO experiment's comprehensive set of measurements of cloud dynamics, surface fluxes, and boundary layer structures (Rauber et al., 2007) provides an ideal setup to evaluate shallow cumulus convection simulations and has been used extensively in previous LES studies (Matheou & Chung, 2014; vanZanten et al., 2011).

Our model reproduces the key features of this marine boundary layer. The time evolution of the boundary layer height (z_i), LWP, and cloud cover (CC) fraction all agree well with the ensemble mean values reported by vanZanten et al. (2011, Figure 4). These quantities exhibit large variations in the first hour of simulation because the model is still in the θ_l spin-up phase. From 03:00 to 24:00, CC fraction remains relatively constant while the LWP increases because of deepening of the cloud layer. With

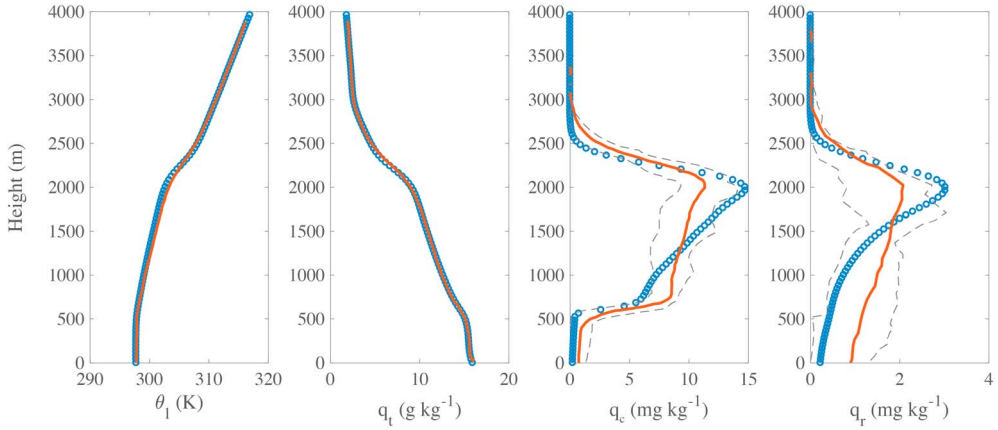

Figure 5. Profiles of the liquid water potential temperature θ_l, total water specific humidity q_t, cloud water specific humidity q_c, and rainwater specific humidity q_r for the period 21:00–24:00 in Run A. The blue circles denote our simulation results. The red lines depict ensemble-averaged vertical profiles from 12 different LES codes from vanZanten et al. (2011), and the gray dashed lines represent the spread of their model ensemble. LES = large eddy simulation.

continued sensible heat input from the ocean surface, the boundary layer grows steadily with time. The horizontal and time-averaged vertical profiles of liquid water potential temperature (θ_l) and total water specific humidity (q_t) also agree well (Figure 5).

Simulated condensed cloud water (q_c) and rainwater (q_r) specific humidities mostly fall within the bounds of the intermodel variability in vanZanten et al. (2011) (Figure 5). Between the heights of 600 and 2,000 m, q_c increases with increasing height at a significantly higher rate than does the ensemble mean of the 12 models in vanZanten et al. (2011), resulting in a 20% higher q_c at the height of 2,000 m. On the other hand, although higher q_r is found near the height of 2,000 m, lower q_r is found near the surface, suggesting a slightly higher raindrop reevaporation rate in our simulation (Figure 5). One possible reason for the difference includes the cloud microphysics parameterization. The ensemble mean value reported by vanZanten et al. (2011) is obtained from 12 different LES codes that use three different microphysical schemes, none of which include the Morrison microphysics scheme used in this study.

4.2. Isotope Features

We now change focus to results from Run B. In the results presented here, all isotopic compositions are expressed in delta notation in reference to the Vienna Standard Mean Ocean Water standard from the specific humidity variable for normal water and the corresponding specific humidity variable for the minor isotope species. For example, the D/H and $^{18}O/^{16}O$ ratios of water vapor are computed following equation (58). We use subscript v, c, and r to denote the isotopic ratios (δ) of water vapor, cloud water, and rainwater, respectively.

Figure 6 shows the diurnal variation of horizontal and hourly-averaged vertical profiles of specific humidity and isotope ratios for water vapor, cloud water, and rainwater from Run B. In the cloudy layer, the horizontal-averaging process implies averaging over regions with and without clouds, and the hourly-averaging removes the time evolution of individual clouds. As expected, the vertical profiles of q_v and δ_v have a negative gradient and d_v shows a positive gradient across the ABL top from 06:00 to 15:00 LST, imposed by the initial conditions. As the boundary layer grows throughout the day, these gradients ensure entrainment of dry, isotope depleted but high d_v air from the free atmosphere into the ABL. Unlike the unsaturated subcloud layer where q_v is well mixed (e.g., Maronga et al., 2014), q_v diminishes with height in the cloud layer (i.e., the layer where $q_c > 0$, Figure 6b). The δ_v profiles also fall off with height in the cloud layer, but the d_v profiles do not. The lack of d_v sensitivity to cloud formation is expected because equilibrium fractionation affect d_v only weakly. In this particular simulation, evaporation of falling raindrops (equations (50)–(52)) has negligible effect on d_v in the unsaturated subcloud layer because the rainwater specific humidity is several orders of magnitude smaller than the water vapor specific humidity (Figures 5 and 6).

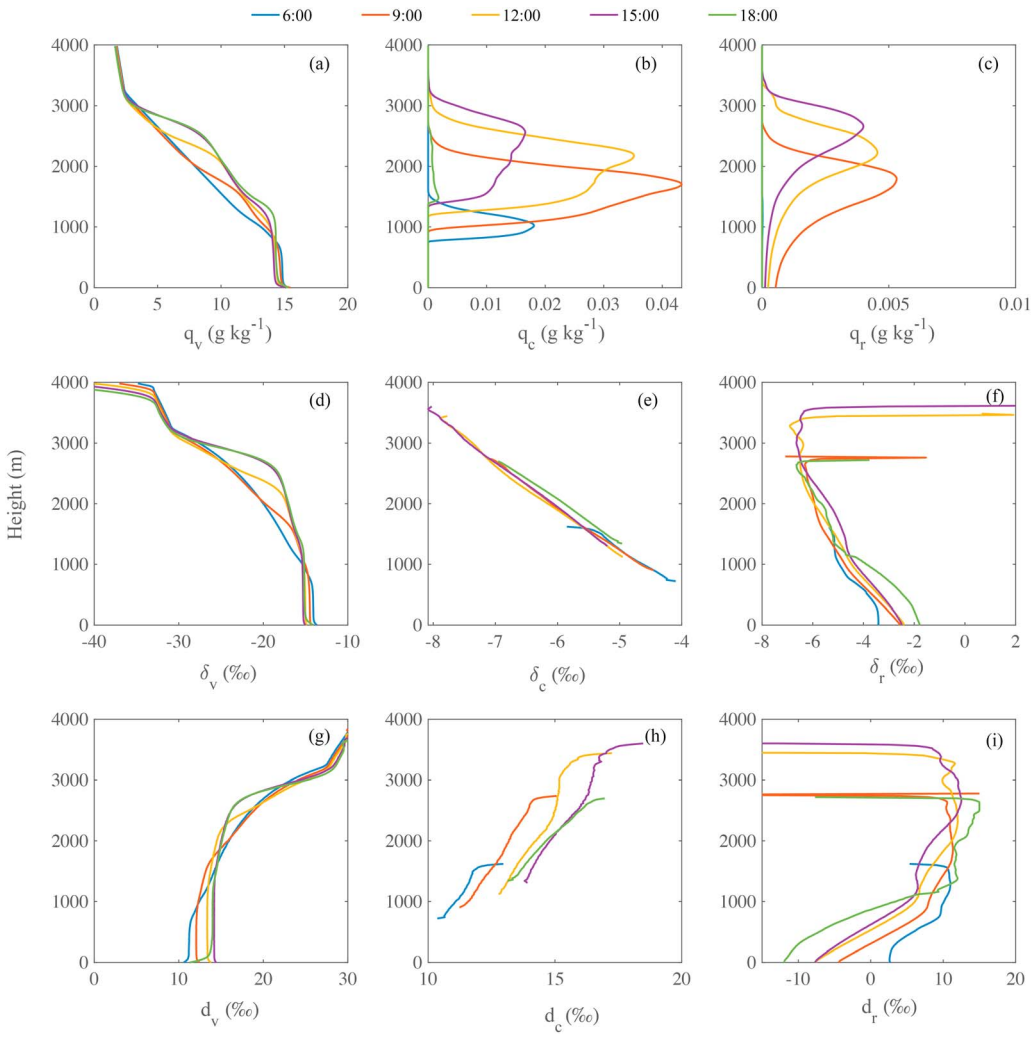

Figure 6. Horizontal- and hourly-averaged evolution of vertical profiles of (a) water vapor specific humidity, (b) cloud water specific humidity, (c) rainwater specific humidity, and of their ^{18}O isotopic compositions (d–f) and deuterium excess (g–i) in Run B.

Figure 7 compares the horizontal- and hourly-averaged LES results for Run B, presented in a δ_v versus q_v parameter space; this figure also includes the theoretical Rayleigh distillation, a mixing line between surface and free-tropospheric values, and reversible moist adiabatic curves (Galewsky et al., 2016). For clarity, only results at 06:00, 9:00, 12:00, 15:00, and 18:00 are shown. The theoretical curves describe results from a well-known box model that is widely used as a basis to identify sources of atmospheric moisture from the combination of vapor isotope ratio δ_v and vapor specific humidity q_v (Conroy et al., 2016; Noone, 2011, 2012; Risi et al., 2010; Worden et al., 2007). Rayleigh distillation is an irreversible pseudo-adiabatic process in an open system (Bailey et al., 2015; Lee & Fung, 2008; Merlivat & Jouzel, 1979; Noone, 2012), whereby some of the liquid water (raindrops) formed during the adiabatic cooling is removed immediately from the system by precipitation and the remaining liquid water remains in isotopic equilibrium with the vapor in the system (Kendall & Caldwell, 1998).

The $q_v - \delta_v$ relationship at 06:00 is essentially that of the initial conditions prescribed to follow the Rayleigh distillation curve (equation (66)). As the clouds form and deepen over time, the $q_v - \delta_v$ relationship shifts closer to the moist adiabatic line and the mixing line; however, the curves do not quite reach the moist adiabatic limit, even in the cloud layer (q_v from 5 to 14 g/kg at 12:00 and 9 to 13 g/kg at 18:00) because the subcloud layer air entering the cloud alters the within cloud $q_v - \delta_v$ relationship. This departure from the moist adiabatic limit is consistent with the satellite-based results of Yoshimura et al. (2011)

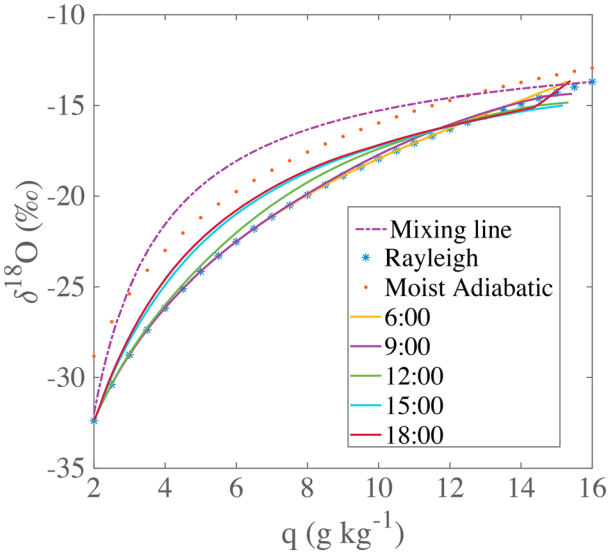

Figure 7. Comparison of the time evolution of the ^{18}O isotopic composition of water vapor in Run B against theoretical predictions. The Rayleigh curve (asterisk) represents a pseudo-adiabatic process. The case of a reversible moist adiabatic process is shown as red dots. The dashed purple curve is a mixing line between surface values and free troposphere. The solid lines represent the time variation of $q_v - \delta_v$ horizontally averaged and 1-hr-averaged vertical profiles.

who suggest that water vapor in the cloud layer is isotopically influenced by nonfractionating air mass mixing. The fact that δ_v values are lower than the moist adiabatic limit reflects downward entrainment of the isotopically lighter water vapor from the free atmosphere into the unsaturated subcloud layer. Raindrop evaporation can also lower δ_v below the cloud layer (q_v from 13 to 16 g/kg). However, as mentioned previously, the role of raindrop evaporation should be negligible compared to that of entrainment because of the drastically different magnitude of rainwater versus water vapor specific humidity.

Vertical profiles of the cloud water specific humidity illustrate the time evolution of the cloud layer (Figure 6b). From 06:00 to 15:00 LST, the cloud layer becomes progressively deeper and higher. The isotopic composition of the cloud water δ_c generally decreases with increasing altitude and evolves negligibly throughout the diurnal cycle (Figure 6e).

The isotopic composition of raindrops δ_r shows distinct patterns in the saturated cloud layer and the unsaturated subcloud layer (Figure 6f). In the cloud layer, δ_r is dominated by both equilibrium fractionation and kinetic processes in raindrop sedimentation, accretion, autoconversion of cloud droplets, and raindrop reevaporation. Here δ_r in this layer exhibits great height variations. In the subcloud layer (800–1,400 m), the vapor-rain isotopic exchanges increase δ_r, resulting in a profile similar to the vertical pattern of δ_v. These findings are consistent with the results of a subcloud evaporation isotopic model designed by Salamalikis et al. (2016). A further enrichment of δ_r and depletion of d_r induced by strong kinectic fractionation occurs as the raindrop gets closer to the ground surface. This pattern differs from that in observational studies of prolonged rain events where the rainwater is generally in equilibrium with the vapor near the ground (Lee et al., 2006). In the present case, the rainwater isotopic composition can deviate from the expected equilibrium value (about −5.5‰) by up to 3‰. At the ground level, d_r is negative.

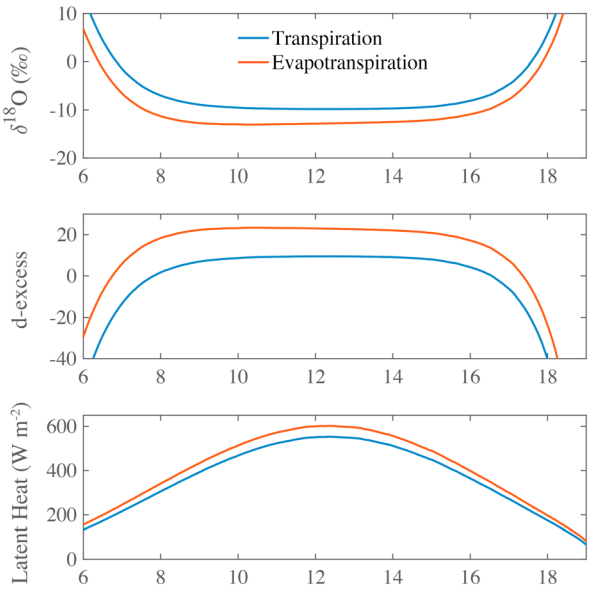

Figure 8. Diurnal variation of the transpiration and evapotranspiration (bottom) and their isotope ratio $\delta^{18}O$ (top) and d (middle) in Run C.

Figure 8 shows the diurnal cycles of $H_2{}^{18}O$ isotope composition, deuterium excess, and heat flux of transpiration and ET for the cloud-free run (Run C). The δ of transpiration decreases gradually from 15‰ at 6:00 to about 10‰ at 9:00, stays at a constant value until around 15:00, and then increases gradually afterward; the d of transpiration mirrors the pattern for δ. These subday patterns are consistent with non–steady state behaviors of canopy transpiration observed in field studies (X. Lee et al., 2007; Zhao et al., 2014). X. Lee et al. (2007) showed a clear, robust diurnal cycle of transpiration δ of a mixed forest, characterized by high values in nocturnal hours, rapid transitions in the early morning and late afternoon, and low values at midday. Zhao et al. (2014) and Welp et al. (2012) found that d of vapor in the surface air layer shows a clear pattern of high values at midday and low values in the early morning and later afternoon. Simulations using an isotope LSM configured for crop systems (corn and soybean) suggest that this vapor d pattern is consistent with either transpiration or entrainment source (Welp et al., 2012).

In this model configuration (Run C), soil evaporation contributes about 15% to the total ET. As a result, δ and d of ET are 4‰ lower and 10‰ higher than those of transpiration, respectively. These results confirm that even a relatively small contribution from evaporation can substantially impact the ET isotopic composition (Huang & Wen, 2014; Welp et al., 2012).

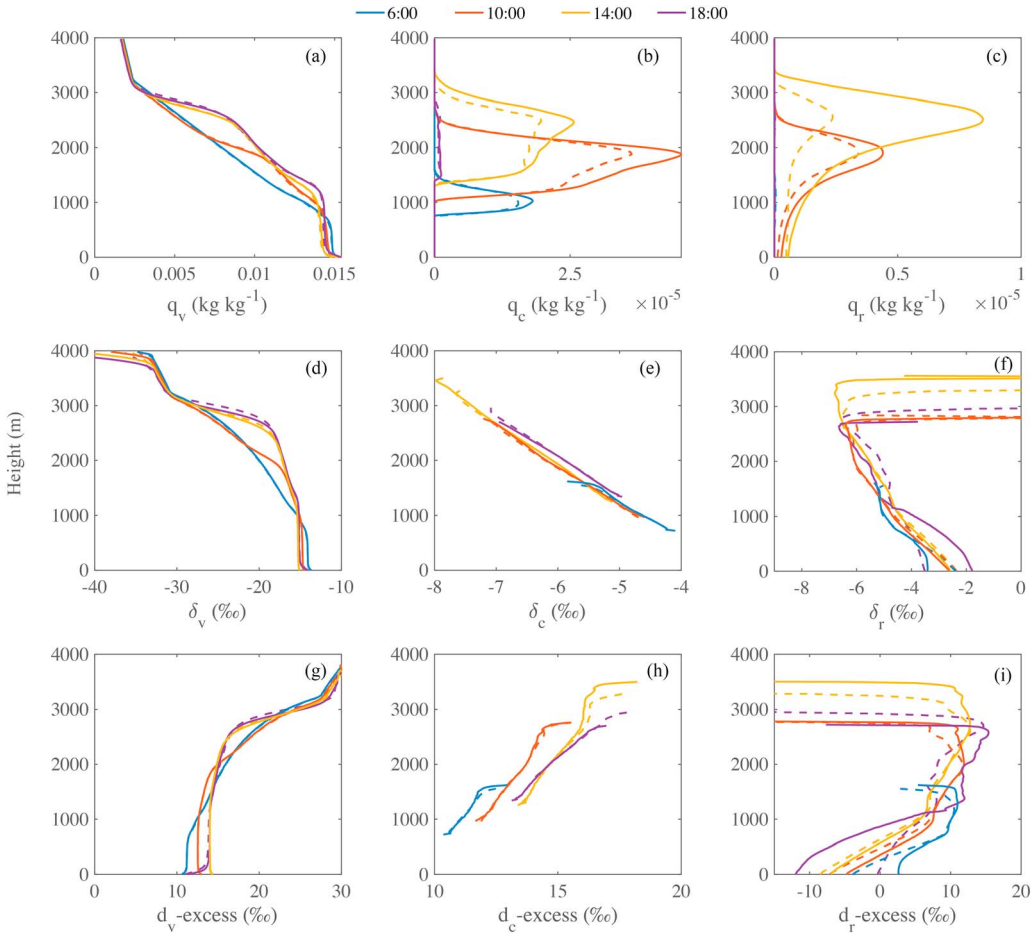

Figure 9. Comparisons of different resolution (solid lines for Run B and dash lines for Run E, respectively) on evolution in time of horizontally averaged vertical profiles of (a) water vapor specific humidity, (b) cloud drop in specific humidity, (c) raindrop in specific humidity, and their $\delta^{18}O$ (d–f) and *d*-excess (g–i) values between 06:00 and 18:00. The time averaging involves a 1-hr average presented at 4-hr intervals in local time.

5. Model Sensitivity Experiments

5.1. Sensitivity to Mesh Resolution

To capture large eddy motion and the structure of the overlying inversion, a sufficiently fine grid mesh resolution is required (Sullivan & Patton, 2011). To investigate the influence of mesh resolution on isotope properties of the ABL water, we describe here a comparison of two simulations (Run B and Run E) that differ in mesh resolution but are otherwise identical (Table 1). Run B utilizes 256 × 256 × 200 grid points with a mesh size of 25 × 25 × 20 m, a resolution that has been demonstrated to produce less grid dependent third-order statistics for nonprecipitating convective boundary layer simulations (Sullivan & Patton, 2011). Run E utilizes 128 × 128 × 100 grid points with a larger mesh size of 50 × 50 × 40 m.

Overall, the vapor specific humidity q_v is relatively insensitive to mesh resolution, with the relative difference being less than 3% between the two mesh resolutions below the height of 2,000 m (Figure 9). In contrast, cloud and rainwater specific humidity q_c and q_r increase with finer resolution. Cloud fraction and LWP also increase in the fine-resolution simulation: at 14:00 the CC fraction is 0.22 and the LWP is 49 g/m^2 in the fine-resolution simulation, whereas the corresponding values are 0.19 and 34 g/m^2 in the coarse-resolution simulation. These results are supported by several other LES simulations showing CC and LWP increase with refinement of grid size (Matheou & Chung, 2014; Stevens, 2002; Stevens et al., 2002, 2005; Yamaguchi & Randall, 2012). These mesh-dependent behaviors are likely related to a combination of the all-or-nothing assumption for condensation and evaporation and the ability for the higher-resolution grid to resolve

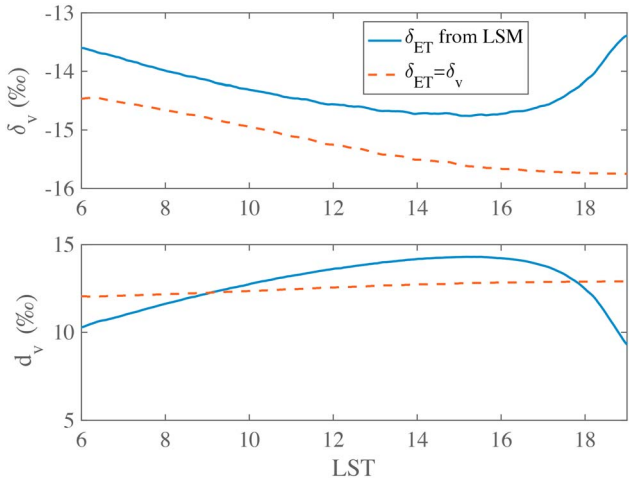

Figure 10. Comparison of time series of near surface (20 m) water vapor δ_v (top) and d_v (bottom) based on different ET isotope ratios (Run C: solid lines and Run D: dash lines). LSM = land surface model; ET = evapotranspiration.

sharp gradients. Matheou and Chung (2014) also found an insensitivity of q_v to grid resolution for the RICO case, but unlike our results, they also found liquid water content to be insensitive to grid size, a result that speaks to differences in the parameterizations of microphysical and subgrid-scale turbulence, as well as in the discretization of scale advection. Large-scale horizontal advection is turned off for all runs except Run A because our study focuses on isotopic simulations in a nearly closed system to avoid *contamination* by water sources of unknown isotopic composition.

Even though there are significant differences in simulated cloud water specific humidity variables (q_c), isotopic quantity δ_c appears relatively insensitive to grid resolution, with differences less than 0.1‰ between Runs B and E at a height of 2,000 m. This is related to the assumption of isotopic equilibrium between cloud liquid and water vapor and the approximate grid independence of water vapor and its isotopic composition. Rainwater isotopic composition is also relatively grid independent in the cloud layer since rain formation through autoconversion and accretion of cloud liquid is nonfractionating. As a result, the cloud isotope ratios become largely resolution independent. Apparently, the insensitivity is a clear limitation in using isotopes to diagnose cloud humidity biases in LES models. On the other hand, the subcloud raindrop reevaporation effect is highly sensitive to resolution. Relatively speaking, isotopic kinetic fractionation between the rain and the ambient vapor becomes more important with finer mesh resolution. Similar to our cloud droplet results, the nonfractionating process of rain-vapor water exchange becomes more important for δ_r in the cloud layer than in the subcloud layer. In comparison δ_v does not exhibit resolution sensitivity.

5.2. Land Surface and Entrainment Impacts

Several observational studies have shown that the diurnal variation of near surface δ_v is lowest and the d_v is highest during the afternoon (Angert et al., 2008; Lai & Ehleringer, 2011; Welp et al., 2012; Wen et al., 2010). The physical processes driving these diurnally varying isotopic cycles include (i) equilibrium and kinetic fractionation during in-cloud condensation and rainout processes; (ii) mixing of different air masses with different δ and d values; (iii) entrainment of the free atmospheric air into the boundary layer; (iv) the addition of moisture from surface ET; and (v) partial evaporation of raindrops below the cloud base (Lai et al., 2006; Lai & Ehleringer, 2011; Welp et al., 2012). Because multiple processes occur simultaneously under natural conditions, it is difficult to determine which process dominates from observational studies.

Here we interrogate two cloud-free and large-scale advection-free simulations (Runs C and D), where the goal is twofold: (a) to demonstrate that the ISOLESC model reproduces these near-surface diurnal patterns of the vapor isotope compositions and (b) to isolate the relative contribution of entrainment and surface ET. In these two runs (C and D), changes to the boundary layer water vapor are controlled solely by vertical mixing and ET. The primary difference between these runs is that the ET isotope ratios in Run C are predicted by the LSM, which accounts for the non–steady state behaviors of plant transpiration and soil evaporation, but those in Run D are forced equal to the isotopic compositions of water vapor at the first grid point above the surface, an arrangement that eliminates the influence of ET on boundary layer vapor isotopic composition. Without land surface isoforcing on the boundary layer (Run D), the near-surface δ_v is about 1‰ lower than the case including land surface isoforcing (Run C), and δ_v and d_v show a slight decreasing and increasing trend with time, respectively, with no apparent diurnal cycle (Figure 10). On the other hand, Run C reveals a clear diurnal cycle: δ_v is lowest in the afternoon and highest in early morning and in the evening, with an amplitude of change of 1.2‰, and d_v is highest in the afternoon and lowest in early morning and in the evening, with an amplitude of change of 5.0‰. These patterns are consistent with Lai and Ehleringer (2011), Lai et al. (2006), and Welp et al. (2012).

A comparison of these two simulations reveals the relative roles of entrainment and land surface ET on water vapor isotopes. During the morning growth of the ABL, free-tropospheric water vapor with low δ_v and high d_v

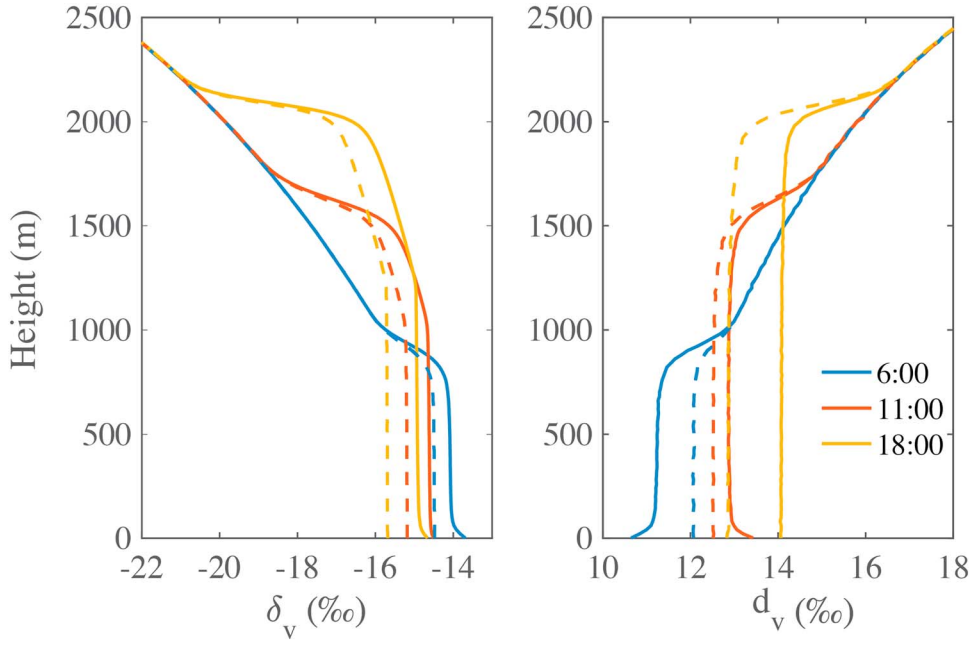

Figure 11. Comparison of vertical profiles of water vapor δ_v (left) and d_v (right) based on different ET isotope ratios (Run C: solid lines and Run D: dashed lines, respectively). The time averaging involves a 1-hr average presented in local time. Note that RH varies with height. ET = evapotranspiration; RH = relative humidity.

is entrained into the boundary layer (Welp et al., 2012). Because the influence of land-surface isoforcing is turned off in Run D, entrainment is the sole contributor to the time evolution of δ_v and d_v. In Run D, entrainment decreases δ_v in the subcloud layer by 1.2‰ and increases d_v by 4‰ between 06:00 and 18:00 LST (Figure 11). Run C includes the influence of both entrainment and the land surface sources, which produces a larger decrease of δ_v and increase of d_v in the subcloud layer over the same time period. These results imply that for these atmospheric conditions, the entrainment and land surface effects are, respectively, responsible for 17% and 83% of the changes occurring throughout the day.

5.3. Impact of Isotopic Rain Evaporation Parameterization

Comparing results from Runs B, F, and G permits analysis of the sensitivity of our results to the rainwater evaporation fractionation parameterization under the current atmospheric conditions. As introduced in sections 2.6 and 3, the treatment of isotopic exchange between rain and vapor in Runs B is faithful to the standard water microphysics. Run F uses an effective relative humidity as the input for the isotopic fractionation equation, which is a common approach in isotope-enabled GCM models. Run G follows the reversible Rayleigh distillation mechanism, whereby the raindrops and the vapor are in isotopic equilibrium and no kinetic fractionation takes place.

Figure 12c shows vertical profiles of δ_r at 15:00 from these three runs. In the reversible Rayleigh case (Run G), δ_r is rapidly enriched with decreasing height ($\delta_r = -6.9$‰ at 3,000 m and $\delta_r = -0.5$‰ at the surface) because of raindrop reevaporation during its descent below cloud base toward the surface, whereas d_r is not affected during the transport. Although deuterium excess is not totally conserved in Rayleigh condensation, in the present case it is approximately constant because only a small segment of the Rayleigh curve is traversed during rain reevaporation. Therefore, Run G exhibits the highest near-surface d_r. However, the assumption that neglecting the effects of subsaturation (i.e., kinetic fractionation) during evaporation is not totally realistic. Run B produces increased δ_r and strong depletion of d_r near the surface compared to Run G. These patterns make sense since the evaporation process tends to reduce d_r and increase δ_r. However, the unreasonably negative d_r (−8‰) at the ground level suggests that the kinetic fractionation may be too strong in the reevaporation calculation in Run B. Another possibility for this negative bias is that the wind shear in this simulation is quite strong (mean geostrophic wind 8.0 m/s at the height of 1.5 km), causing the rain to fall outside

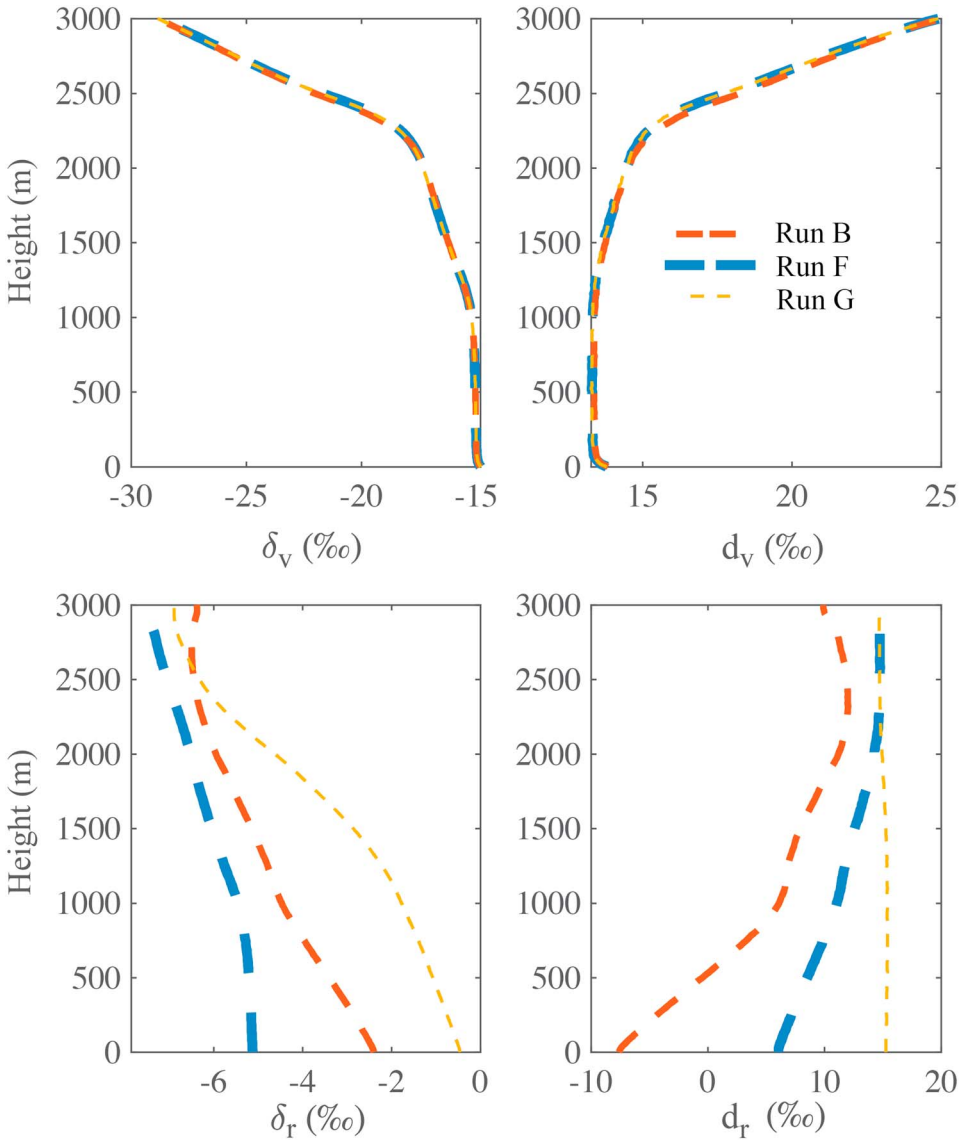

Figure 12. Vertical profile of water vapor/precipitation isotope ratio δ and d according to the kinetic fractionation estimated from a local treatment without tunable parameters (Run B: red line), effective relative humidity used in GCM (Run F: blue line), and reversible Rayleigh distillation (Run G: yellow line) at about 12:00. GCM = global climate model.

the cloud and therefore undergo unusually large kinetic fractionation. As Figure 13 shows, the resolved RH in the cloud layer (at a height of 1000 m) and in the subcloud layer (at a height of 200 m) differs by about 25%, causing strong kinetic fractionation during the raindrop descent. Using an effective humidity parameterization (equation (57), Run F) produces a more realistic near-surface d_r (7‰). The improvement suggests that even in such a high-resolution simulation, the conditions around the raindrop are not resolved, especially below the cloud layer. These different kinetic fractionation parameterizations have a negligible effect on the isotopic compositions of water vapor (Figure 12), which again results from the fact that there are several orders of magnitude more water vapor mass than raindrop mass (Figure 6).

Nevertheless, this sensitivity analysis confirms that below the cloud layer the kinetic effect exerts strong influences on the isotopic composition of precipitation reaching the ground (Hoffmann et al., 2000). Previous studies on raindrop reevaporation deploy large grid sizes typical of a GCM (~100 km) or a regional model (~5 km) and use the partial equilibration RH relationship to represent unresolved RH variations. This assumption is useful but at the same time makes raindrop isotope composition less sensitive to microphysical

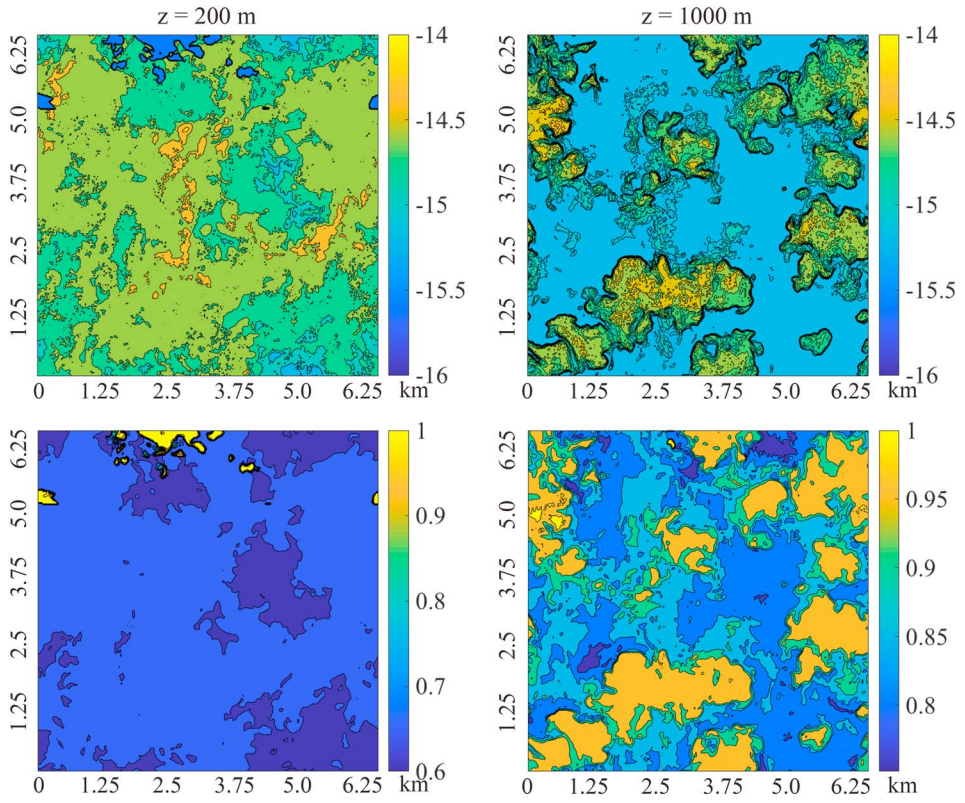

Figure 13. Resolved vapor $^{18}O/^{16}O$ ratio and relative humidity at 12:00 at 200 m (left) and 1,000 m (right) in Run B. Contour intervals are different between the panels.

parameterization. Our model does not require tunable parameters for isotopic microphysical parameterizations and thus may help constrain parameterizations in large-scale models.

6. Discussion

ISOLESC is a tool for investigating the interplay between various processes involved in the atmospheric water cycle, by using the additional constraints provided by the stable isotopes of water. In this regard, it is complementary to other isotope-enabled atmospheric models, including GCMs (Nusbaumer et al., 2017; Yoshimura et al., 2008), regional climate models (Yoshimura et al., 2010), and cloud resolving models (CRMs) (Blossey et al., 2010). Each class of these isotope-enabled models has its strengths and limitations. Although GCMs and CRMs are widely used to investigate the impact of continental recycling (Risi et al., 2013), vapor source identification (Wei et al., 2016), and air-rain isotopic exchange (Lee & Fung, 2008), their coarse resolutions ($>$ 10 km) do not allow explicitly resolved atmospheric convection. Blossey et al. (2010) overcame this weakness by using cloud-resolving simulations with horizontal resolutions of about 2.5 km^2 along with a variable vertical grid spacing of 75–300 m, demonstrating large impacts of deep convection and cirrus cloud formation on the isotopic compositions of water vapor near the tropopause. However, the resolutions of CRMs are still too coarse to resolve turbulent fluxes and the exchange between the ABL and the free atmosphere.

By design, ISOLESC can handle boundary layer transport processes that other isotope-enabled atmospheric models cannot. For example, entrainment at the top of the boundary layer is explicitly resolved in ISOLESC. So ISOLESC can quantify the influence of the free-atmospheric vapor on the variability of the vapor isotopic composition near the surface (Figure 10). This free-atmospheric influence is a source of uncertainty in determining the isotopic composition of surface ET from the Keeling mixing model (Lee et al., 2011). In principle, ISOLESC can be used to correct this error if the free-atmospheric δ_v is known.

ISOLESC can also be used to interrogate the influence of isotopic spatial variations produced by organized turbulent motions in the ABL. An example is shown in Figure 13. Although the vertical variation of mean δ_v

is fairly uniform in the boundary layer (Figure 9), organized turbulent motions create large variations at the resolved eddy scales. At a height of 1,000 m, clouds (RH $>$ 97%) occupy about one third of the horizontal domain in the example shown in Figure 13. Contrary to conventional belief, the within-cloud vapor isotopic composition is not homogeneous; instead, it can vary by up to 1‰ for ^{18}O (for the conditions simulated here). In the subcloud layer (at a height of 200 m), pockets of high δ_v are evident (Figure 13), presumably resulting from raindrop reevaporation.

Using the isotope-enabled Community Atmosphere Model, Nusbaumer et al. (2017) found that large uncertainties in water isotope ratios in the atmosphere result not only from insufficient resolution but also from the model physics itself. The isotopic representation of cloud processes is one of the major sources of uncertainty. In this study, isotopic exchange of vapor, cloud liquid, and rain was added to a two-moment microphysics scheme, which should improve the parameterization of cloud processes over models that use one-moment microphysics schemes. Galewsky et al. (2016) and Pfahl et al. (2012) argue that two-moment schemes are superior to one-moment schemes because the latter is essentially a bulk parameterization that does not differentiate droplet size classes.

Another modeling uncertainty relates to isotopic fractionation of evaporating raindrops and representation of cloud microphysics. In the unsaturated subcloud layer, precipitation isotope ratios are highly sensitive to the relative humidity of the air surrounding the reevaporating raindrops and to the fraction of raindrops that reevaporate (Bony et al., 2008; Salamalikis et al., 2016; Stewart, 1975). With notably smaller grid meshes (~25 m) than typically used in larger-scale weather, cloud-resolving, and climate models (~1 to100 km), the ISOLESC d_r simulation results are still too negative compared to reality. Since isotopic fractionation of evaporating raindrops has been well studied (Bony et al., 2008; Lee & Fung, 2008; Salamalikis et al., 2016; Stewart, 1975), this bias could be attributed to too strong reevaporation rate in Morrison two-moment cloud microphysical scheme and the fact that conditions around the falling raindrop in the subcloud layer are not fully resolved. It is worth noting that the particular case simulated here is synthetic and is not constrained by observations.

Most previous water isotope models assume that ET over land occurs without fractionating against the heavier water isotopes; this assumption is justified on time scales of days to weeks since mass conservation requires (1) that the isotope compositions of the evaporated water be equal to those of the source water on these time scales or (2) that an isotopic steady state be maintained (Griffis et al., 2011). However, it is well known from experimental studies that plant transpiration and soil evaporation exhibit non–steady state behaviors at subdaily time scales (Lai & Ehleringer, 2011). Our ISOLESC simulations confirm that the non–steady state behaviors can play a large role in the water vapor isotopic variability in the ABL through the course of the day. Omission of the fractionation mechanism during ET may be a key reason for why GCMs have difficulty reproducing the observed near-surface water vapor isotopic composition, especially for deuterium excess.

A drawback of ISOLESC is that it requires that the isotopic composition of free-atmospheric vapor be specified through the initial profiles (Figure 3). Although it is reasonable to assume that the initial vapor ^{18}O profile follows the Rayleigh relation with the initial specific humidity in the boundary layer (equation (66), Bailey et al., 2013), the use of an observed vapor deuterium excess (d_v) profile in the northeast United States (He & Smith, 1999) as the initial condition is somewhat arbitrary. The aircraft measurements of He and Smith (1999), which appears to be the only published data set on d_v profiles in the boundary layer, show that d_v is 18‰ greater in the free atmosphere than in the boundary layer, but it is unknown whether the free-atmospheric vapor always has higher d_v than vapor in the ABL. Free-tropospheric profiles could also be drawn from isotope-enable GCMs. However, these profiles have not been validated by observation. Direct measurements of d_v above the boundary layer are urgently needed to improve the realism of ABL isotope modeling.

A second key limitation of ISOLESC relates to having assumed that the atmosphere is incompressible. Although assuming an incompressible atmosphere is appropriate for boundary layer scale studies, this assumption restricts ISOLESC's applicability to shallow-cloud regimes (i.e., regimes with relatively small cloud-induced vertical velocities). Therefore, ISOLESC is not appropriate for studying the influence of deep convection on isotopic variations.

While the present study reports ISOLESC simulation results with an atmosphere configured to produce precipitating shallow cumulus clouds (i.e., RICO), ISOLESC has also been configured to simulate regimes

dominated by nonprecipitating shallow cumulus clouds (SGP97, Brown et al., 2002 and Lohou & Patton, 2014) and stratocumulus (Moeng, 2000)

7. Conclusions

The backbone of ISOLESC is the NCAR LES. Key features of ISOLESC include the following: (1) parameterization of non–steady state isotopic behaviors of plant transpiration and soil evaporation, (2) nondiscriminating exchanges of light and heavy water vapor isotopes between the ABL and the free atmosphere via entrainment, (3) equilibrium fractionation associated with cloud related water phase changes using a two-moment cloud microphysics scheme, and (4) kinetic fractionation of raindrops in nonsaturated grid cells and under the cloud layer.

ISOLESC successfully reproduces the standard ABL features observed during the RICO experiment, including the ABL height, the cloud fraction, the LWP, and the vertical distributions of cloud and rainwater specific humidity. The simulated time evolution of the water vapor isotopic composition and the vapor specific humidity in the ABL matches reasonably well with the theoretical curves expected of the moist adiabatic and mixing processes. The diurnal changes in the near-surface vapor ^{18}O composition and deuterium excess broadly agree with observed patterns. For the current configuration, nondiscriminating entrainment only contributes 17% to the subdaily time variation of near-surface vapor deuterium excess, and fractionation associated with surface ET contributes 83%.

Our model simulations demonstrate the sensitivity of ABL properties to mesh size and isotopic parameterizations. The grid size has appreciable effect on the cloud water specific humidity but little impact on the predicted isotopic compositions of water vapor and cloud droplet. The rainwater specific humidity and its isotope ratios are highly sensitive to resolution, as a result of different saturation conditions between fine and coarse resolutions. This isotopic analysis of raindrops confirms that the kinetic effect exerts strong influences on the isotopic composition of precipitation reaching the ground.

Because entrainment of free-tropospheric air into the ABL participates substantially in controlling the temporal evolution of the ABL's water vapor composition (Sodemann et al., 2017), the initial condition for water vapor isotopic composition imposed in the free troposphere strongly impacts ISOLESC results. Direct measurements of d_v above the boundary layer are urgently needed to improve the realism of ABL isotope simulation and hence the community's understanding of the processes controlling water isotopes in the ABL. Allowing soil moisture isotope ratios to evolve during the simulation might also prove beneficial.

Appendix A

The notations used in this study are shown in Table A1, and site information and initial settings of the isotope-enabled land surface model are described in Table A2.

Table A1
List of Symbols and Their Definition

Notation	Description
A and B	the thermodynamic parameters related to the release of latent heat
a_r and b_r	fall speed parameters for rain
$\mathbf{B}$	subfilter-scale fluxes of temperature
c_m	Prandtl number for SFS motions
C	the condensation rate
CC	cloud cover
C_p	the specific gas constants for heat capacity
d	deuterium excess
D_v	the molecular diffusivities of normal vapor
D_{v_i}	the molecular diffusivities of isotopic vapor
D_p	particle diameter of drop
$\mathscr{D}$	SFS diffusion
e	subfilter-scale (SFS) turbulent kinetic energy
E	soil evaporation
f	Coriolis parameter

Table A1 *(continued)*

Notation	Description
f_1 and f_2	ventilation parameters
g	Earth's gravitational acceleration
l	stability-dependent mixing length
LAI	leaf area index
LWP	liquid water path
M	the microphysical source/sink terms
n	the degree of freedom
N	number concentration
$\mathbf{N}$	subfilter-scale fluxes of cloud/rain droplets
N_0	intercept parameter in size distributions of the cloud droplets calculation
N_b	Brunt-Väisälä frequency
p	time-invariant hydrostatic mean pressure
p_0	a standard reference pressure
P	Péclet number
$\mathscr{P}$	SFS shear
q	specific humidity
q_s	saturation specific humidity
$\mathbf{Q}$	subfilter-scale fluxes of specific humidity
r_t	total resistance to the diffusion of water vapor
R	the ratios of the mass of the heavier isotope to the normal water
RH_c^*	relative humidity expressed as a fraction in reference to the canopy temperature
R_{dry}	the specific gas constants for dry air
RH_e	the effective relative humidity
RH_{grid}	the resolved relative humidity
RH^*	relative humidity in reference to the temperature of the soil
S	liquid water saturation ratio
S_c	Schmidt number
subscript $_c$	cloud
subscript $_e$	equilibrium
subscript $_i$	isotope
subscript $_l$	liquid water
subscript $_r$	rain
subscript $_v$	water vapor
subscript $_t$	total
subscript $_{aac}$	accretion of cloud droplets by rain
subscript $_{act}$	droplet activation of aerosols
subscript $_{auto}$	autoconversion of cloud droplets to rain
subscript $_{con}$	water condensation
subscript $_{evap}$	droplet evaporation
subscript $_{sed}$	droplet sedimentation
subscript $_{self}$	self-collection of cloud water
T	absolute temperature
T	SFS momentum fluxes
Tr	canopy transpiration
$\mathbf{u}$	three-dimension velocity
U_g	the geostrophic wind
W	the leaf water content
w_i	the mole fraction of water vapor in the intercellular space
$\overline{w'q'_v}$	the ET flux computed by the LSM
z_i	the boundary layer height
α_e	the equilibrium isotope fractionation factor
β	the buoyancy parameter
δ	delta values of isotopic ratio
δ_s	delta values of soil water isotopic ratio
$\delta_{L,\,e}$	δ of the water at the evaporating site in the leaves in non–steady state
$\delta_{L,\,es}$	δ of water at the evaporating site in the leaves in steady state
$\mathscr{E}$	SFS dissipation
ε	a tunable parameter representing the fraction of the rain droplets reaching the isotopic equilibrium state

Table A1 *(continued)*

Notation	Description
ε_k	the isotopic kinetic fractionation
$\hat{k}$	the unit vector in the vertical direction z
λ	Slope parameter in size distributions of the cloud droplets calculation
π	pressure
Γ	Euler gamma function
μ_a	the dynamic viscosity of air
θ_{v_0}	the reference virtual potential temperature
θ_l	the liquid water potential temperature
υ_H	the turbulent diffusivity
υ_M	the turbulent eddy viscosity
Δ	the filter scale
μ	shape parameter in size distributions of the cloud droplets calculation
$\mathscr{B}$	buoyancy production
Π	the Exner function

Note. ET = evapotranspiration; LSM = land surface model.

Table A2
Site Information and Initial Settings of the Isotope-Enabled Land Surface Model

Site information	Description
Longitude	90.5°
Latitude	36.62°
Altitude	320 m
Land cover	Grassland
Parameters	
Leaf area index	4 m^2/m^2
Soil type	Clay loam
Albedo	0.2
Areal fractional coverage of green vegetation	0.9
Roughness length	0.1 m
Minimum canopy resistance	s/m
Soil temperature at 0.05 m	298.28 K
Soil temperature at 0.2 m	298 K
Soil temperature at 0.6 m	293.73 K
Soil temperature at 1.0 m	290.92 K
Soil moisture at 0.05 m	0.441 m^3/m^3
Soil moisture at 0.2 m	0.419 m^3/m^3
Soil moisture at 0.6 m	0.338 m^3/m^3
Soil moisture at 1.0 m	0.348 m^3/m^3
Soil isotope ratios	−10‰ and − 70‰ for δ^{18}O and δD
Péclet number	2.3×10^{-9}
Leaf water content	159 g/m^2

Acknowledgments
This work was supported by the U.S. National Science Foundation (grant AGS-1520684). We acknowledge high-performance computing support from Yellowstone (ark:/85065/d7wd3xhc) provided by NCAR's Computational and Information Systems Laboratory, sponsored by the National Science Foundation. All the data used in this study are available upon request from the corresponding author. Critical comments from Adriana Raudzens Bailey on an earlier draft of this manuscript were helpful and appreciated. E. G. P. also acknowledges numerous conversations on this topic with NCAR scientists George Bryan, Wojciech Grabowski, Chin-Hoh Moeng, Hugh Morrison, Rich Rotunno, and Peter Sullivan. NCAR is sponsored by the National Science Foundation.

References

Aemisegger, F., Pfahl, S., Sodemann, H., Lehner, I., Seneviratne, S. I., & Wernli, H. (2014). Deuterium excess as a proxy for continental moisture recycling and plant transpiration. *Atmospheric Chemistry and Physics*, *14*(8), 4029–4054. https://doi.org/10.5194/acp-14-4029-2014

Angert, A., Lee, J.-E., & Yakir, D. A. N. (2008). Seasonal variations in the isotopic composition of near-surface water vapour in the eastern Mediterranean. *Tellus B*, *60*(4), 674–684. https://doi.org/10.1111/j.1600-0889.2008.00357.x

Bailey, A., Noone, D., Berkelhammer, M., Steen-Larsen, H. C., & Sato, P. (2015). The stability and calibration of water vapor isotope ratio measurements during long-term deployments. *Atmospheric Measurement Techniques*, *8*(10), 4521–4538. https://doi.org/10.5194/amt-8-4521-2015

Bailey, A., Toohey, D., & Noone, D. (2013). Characterizing moisture exchange between the Hawaiian convective boundary layer and free troposphere using stable isotopes in water. *Journal of Geophysical Research: Atmospheres*, *118*, 8208–8221. https://doi.org/10.1002/jgrd.50639

Beheng, K. D. (1994). A parameterization of warm cloud microphysical conversion processes. *Atmospheric Research*, *33*(1-4), 193–206. https://doi.org/10.1016/0169-8095(94)90020-5

Betts, A. K. (1973). Non-precipitating cumulus convection and its parameterization. *Quarterly Journal Of The Royal Meteorological Society*, *99*(419), 178–196. https://doi.org/10.1002/qj.49709941915

Blossey, P. N., Kuang, Z., & Romps, D. M. (2010). Isotopic composition of water in the tropical tropopause layer in cloud-resolving simulations of an idealized tropical circulation. *Journal of Geophysical Research*, *115*, D24309. https://doi.org/10.1029/2010JD014554

Bony, S., Risi, C., & Vimeux, F. (2008). Influence of convective processes on the isotopic composition (δ18O and δD) of precipitation and water vapor in the tropics: 1. Radiative-convective equilibrium and Tropical Ocean–Global Atmosphere–Coupled Ocean-Atmosphere Response Experiment (TOGA-COARE) simulations. *Journal of Geophysical Research*, *113*, D19306. https://doi.org/10.1029/2008JD009943

Brown, A. R., Cederwall, R. T., Chlond, A., Duynkerke, P. G., Golaz, J. C., Khairoutdinov, M., et al. (2002). Large-eddy simulation of the diurnal cycle of shallow cumulus convection over land. *Quarterly Journal of the Royal Meteorological Society*, *128*(582), 1075–1093. https://doi.org/10.1256/003590002320373210

Chang, S., Hahn, D., Yang, C.-H., Norquist, D., & Ek, M. (1999). Validation study of the CAPS model land surface scheme using the 1987 Cabauw/PILPS dataset. *Journal of Applied Meteorology*, *38*(4), 405–422. https://doi.org/10.1175/1520-0450(1999)038<0405:VSOTCM>2.0.CO;2

Chen, F., Manning, K. W., LeMone, M. A., Trier, S. B., Alfieri, J. G., Roberts, R., et al. (2007). Description and evaluation of the characteristics of the NCAR high-resolution land data assimilation system. *Journal of Applied Meteorology and Climatology*, *46*(6), 694–713. https://doi.org/10.1175/JAM2463.1

Conroy, J. L., Noone, D., Cobb, K. M., Moerman, J. W., & Konecky, B. L. (2016). Paired stable isotopologues in precipitation and vapor: A case study of the amount effect within western tropical Pacific storms. *Journal of Geophysical Research: Atmospheres*, *121*, 3290–3303. https://doi.org/10.1002/2015JD023844

Craig, H., & Gordon, L. I. (1965). *Deuterium and oxygen 18 variations in the ocean and the marine atmosphere*. Spoleto, Italy: Consiglio nazionale delle richerche, Laboratorio de geologia nucleare.

Cuijpers, J. W. M., & Duynkerke, P. G. (1993). Large eddy simulation of trade wind cumulus clouds. *Journal of the Atmospheric Sciences*, *50*(23), 3894–3908. https://doi.org/10.1175/1520-0469(1993)050<3894:LESOTW>2.0.CO;2

Deardorff, J. W. (1980). Stratocumulus-capped mixed layers derived from a three-dimensional model. *Boundary-Layer Meteorology*, *18*(4), 495–527. https://doi.org/10.1007/BF00119502

Delattre, H., Vallet-Coulomb, C., & Sonzogni, C. (2015). Deuterium excess in the atmospheric water vapour of a Mediterranean coastal wetland: Regional vs. local signatures. *Atmospheric Chemistry and Physics*, *15*(17), 10,167–10,181. https://doi.org/10.5194/acp-15-10167-2015

Eltahir, E. A. B., & Bras, R. L. (1996). Precipitation recycling. *Reviews of Geophysics*, *34*(3), 367–378. https://doi.org/10.1029/96RG01927

Emanuel, K. A. (1994). *Atmospheric convection* (580 pp.). New York: Oxford University Press.

Farquhar, G. D., & Cernusak, L. A. (2005). On the isotopic composition of leaf water in the non-steady state. *Functional Plant Biology*, *32*(4), 293–303. https://doi.org/10.1071/FP04232

Galewsky, J., Steen-Larsen, H. C., Field, R. D., Worden, J., Risi, C., & Schneider, M. (2016). Stable isotopes in atmospheric water vapor and applications to the hydrologic cycle. *Reviews of Geophysics*, *54*, 809–865. https://doi.org/10.1002/2015RG000512

Gat, J. R. (2000). Atmospheric water balance—The isotopic perspective. *Hydrological Processes*, *14*(8), 1357–1369. https://doi.org/10.1002/1099-1085(20000615)14:8<1357::AID-HYP986>3.0.CO;2-7

Griffis, T. J. (2013). Tracing the flow of carbon dioxide and water vapor between the biosphere and atmosphere: A review of optical isotope techniques and their application. *Agricultural and Forest Meteorology*, *174*, 85–109.

Griffis, T. J., Lee, X., Baker, J. M., Billmark, K., Schultz, N., Erickson, M., et al. (2011). Oxygen isotope composition of evapotranspiration and its relation to C4 photosynthetic discrimination. *Journal of Geophysical Research*, *116*, G01035. https://doi.org/10.1029/2010JG001514

He, H., & Smith, R. B. (1999). Stable isotope composition of water vapor in the atmospheric boundary layer above the forests of New England. *Journal of Geophysical Research*, *104*(D9), 11,657–11,673. https://doi.org/10.1029/1999JD900080

Hoffmann, G., Jouzel, J., & Masson, V. (2000). Stable water isotopes in atmospheric general circulation models. *Hydrological Processes*, *14*(8), 1385–1406. https://doi.org/10.1002/1099-1085(20000615)14:8<1385::AID-HYP989>3.0.CO;2-1

Huang, L., & Wen, X. (2014). Temporal variations of atmospheric water vapor δD and δ18O above an arid artificial oasis cropland in the Heihe River basin. *Journal of Geophysical Research: Atmospheres*, *119*, 456–476. https://doi.org/10.1002/2014JD021891

Jouzel, J. (1986). Isotopes in cloud physics: Multistep and multistage processes. In P. Fritz & J. C. Frontes (Eds.), *Handbook of environmental isotope geochemistry* (Vol. 2, pp. 61–112). New York: Elsevier.

Jouzel, J., Delaygue, G., Landais, A., Masson-Delmotte, V., Risi, C., & Vimeux, F. (2013). Water isotopes as tools to document oceanic sources of precipitation. *Water Resources Research*, *49*, 7469–7486. https://doi.org/10.1002/2013WR013508

Kendall, C., & Caldwell, E. A. (1998). Fundamentals of isotope geochemistry. In C. Kendall & J. J. McDonnell (Eds.), *Isotope tracers in catchment hydrology* (pp. 51–86). Amsterdam: Elsevier Science B.V. https://doi.org/10.1016/B978-0-444-81546-0.50009-4

Khvorostyanov, V. I., & Curry, J. A. (1999). Toward the theory of stochastic condensation in clouds. Part I: A general kinetic equation. *Journal of the Atmospheric Sciences*, *56*(23), 3985–3996. https://doi.org/10.1175/1520-0469(1999)056<3985:TTTOSC>2.0.CO;2

Lai, C. T., & Ehleringer, J. R. (2011). Deuterium excess reveals diurnal sources of water vapor in forest air. *Oecologia*, *165*(1), 213–223. https://doi.org/10.1007/s00442-010-1721-2

Lai, C. T., Ehleringer, J. R., Bond, B. J., & Paw U, K. T. (2006). Contributions of evaporation, isotopic non-steady state transpiration and atmospheric mixing on the delta O-18 of water vapour in Pacific Northwest coniferous forests. *Plant, Cell & Environment*, *29*(1), 77–94. https://doi.org/10.1111/j.1365-3040.2005.01402.x

Lee, J. E., & Fung, I. (2008). "Amount effect" of water isotopes and quantitative analysis of post-condensation processes. *Hydrological Processes*, *22*(1), 1–8. https://doi.org/10.1002/hyp.6637

Lee, J.-E., Fung, I., DePaolo, D. J., & Henning, C. C. (2007). Analysis of the global distribution of water isotopes using the NCAR atmospheric general circulation model. *Journal of Geophysical Research*, *112*, D16306. https://doi.org/10.1029/2006JD007657

Lee, X., Griffis, T. J., Baker, J. M., Billmark, K. A., Kim, K., & Welp, L. R. (2009). Canopy-scale kinetic fractionation of atmospheric carbon dioxide and water vapor isotopes. *Global Biogeochemical Cycles*, *23*, GB1002. https://doi.org/10.1029/2008GB003331

Lee, X., Huang, J., & Patton, E. G. (2011). A large-eddy simulation study of water vapour and carbon dioxide isotopes in the atmospheric boundary layer. *Boundary Layer Meteorology*, *145*(1), 229–248.

Lee, X., Kim, K., & Smith, R. (2007). Temporal variations of the18O/16O signal of the whole-canopy transpiration in a temperate forest. *Global Biogeochemical Cycles*, *21*, GB3013. https://doi.org/10.1029/2006GB002871

Lee, X., Smith, R., & Williams, J. (2006). Water vapour O-18/O-16 isotope ratio in surface air in New England, USA. *Tellus B*, *58*(4), 293–304. https://doi.org/10.1111/j.1600-0889.2006.00191.x

Lohou, F., & Patton, E. G. (2014). Surface energy balance and buoyancy response to shallow cumulus shading. *Journal of the Atmospheric Sciences*, *71*(2), 665–682. https://doi.org/10.1175/JAS-D-13-0145.1

Majoube, M. (1971). Fractionation in O-18 between ice and water vapor. *Journal de Chimie Physique et de Physico-Chimie Biologique*, *68*(4), 625–636. https://doi.org/10.1051/jcp/1971680625

Maronga, B., Hartogensis, O. K., Raasch, S., & Beyrich, F. (2014). The effect of surface heterogeneity on the structure parameters of temperature and specific humidity: A large-eddy simulation case study for the LITFASS-2003 experiment. *Boundary-Layer Meteorology*, *153*(3), 441–470. https://doi.org/10.1007/s10546-014-9955-x

Matheou, G., & Chung, D. (2014). Large-Eddy simulation of stratified turbulence. Part II: Application of the stretched-vortex model to the atmospheric boundary layer. *Journal of the Atmospheric Sciences*, *71*(12), 4439–4460. https://doi.org/10.1175/JAS-D-13-0306.1

Merlivat, L., & Jouzel, J. (1979). Global climatic interpretation of the deuterium-oxygen 18 relationship for precipitation. *Journal of Geophysical Research*, *84*(C8), 5029–5033. https://doi.org/10.1029/JC084iC08p05029

Mitchell, K. (2005). The Community Noah Land-Surface Model (LSM) users guide public release version 2.7.1. Tech. rep., 1–26 pp.

Moeng, C. H. (1984). A large-eddy-simulation model for the study of planetary boundary-layer turbulence. *Journal of the Atmospheric Sciences*, *41*(13), 2052–2062. https://doi.org/10.1175/1520-0469(1984)041<2052:ALESMF>2.0.CO;2

Moeng, C.-H. (1998). Stratocumulus-topped atmospheric planetary boundary layer. In E. J. Plate, et al. (Eds.), *Buoyant Con- vect. Geophys. flows* (pp. 421–440). Dordrecht, Netherlands: Kluwer Academic Publishers.

Moeng, C.-H. (2000). Entrainment rate, cloud fraction, and liquid water path of PBL stratocumulus clouds. *Journal of the Atmospheric Sciences*, *57*(21), 3627–3643. https://doi.org/10.1175/1520-0469(2000)057<3627:ERCFAL>2.0.CO;2

Moeng, C.-H., & Wyngaard, J. C. (1988). Spectral analysis of large-eddy simulations of the convective boundary layer. *Journal of the Atmospheric Sciences*, *45*(23), 3573–3587. https://doi.org/10.1175/1520-0469(1988)045<3573:SAOLES>2.0.CO;2

Morrison, H., Curry, J. A., & Khvorostyanov, V. I. (2005). A new double-moment microphysics parameterization for application in cloud and climate models. Part I: Description. *Journal of the Atmospheric Sciences*, *62*(6), 1665–1677. https://doi.org/10.1175/JAS3446.1

Morrison, H., & Grabowski, W. W. (2007). Comparison of bulk and bin warm-rain microphysics models using a kinematic framework. *Journal of the Atmospheric Sciences*, *64*(8), 2839–2861. https://doi.org/10.1175/JAS3980

Morrison, H., & Grabowski, W. W. (2008). Modeling supersaturation and subgrid-scale mixing with two-moment bulk warm microphysics. *Journal of the Atmospheric Sciences*, *65*(3), 792–812. https://doi.org/10.1175/2007JAS2374.1

Morrison, H., Thompson, G., & Tatarskii, V. (2009). Impact of cloud microphysics on the development of trailing stratiform precipitation in a simulated squall line: Comparison of one- and two-moment schemes. *Monthly Weather Review*, *137*(3), 991–1007. https://doi.org/10.1175/2008MWR2556.1

Noone, D. (2012). Pairing measurements of the water vapor isotope ratio with humidity to deduce atmospheric moistening and dehydration in the tropical midtroposphere. *Journal of Climate*, *25*(13), 4476–4494. https://doi.org/10.1175/JCLI-D-11-00582.1

Noone, D., Galewsky, J., Sharp, Z. D., Worden, J., Barnes, J., Baer, D., et al. (2011). Properties of air mass mixing and humidity in the subtropics from measurements of the D/H isotope ratio of water vapor at the Mauna Loa Observatory. *Journal of Geophysical Research*, *116*, D22113. https://doi.org/10.1029/2011JD015773

Nusbaumer, J., Wong, T. E., Bardeen, C., & Noone, D. (2017). Evaluating hydrological processes in the Community Atmosphere Model version 5 (CAM5) using stable isotope ratios of water. *Journal of Advances in Modeling Earth Systems*, *9*, 949–977. https://doi.org/10.1002/2016MS000839

Patton, E. G., Sullivan, P. P., & Moeng, C. H. (2005). The influence of idealized heterogeneity on wet and dry planetary boundary layers coupled to the land surface. *Journal of the Atmospheric Sciences*, *62*(7), 2078–2097. https://doi.org/10.1175/JAS3465.1

Patton, E. G., Sullivan, P. P., Shaw, R. H., Finnigan, J. J., & Weil, J. C. (2016). Atmospheric stability influences on coupled boundary layer and canopy turbulence. *Journal of the Atmospheric Sciences*, *73*(4), 1621–1647. https://doi.org/10.1175/JAS-D-15-0068.1

Pfahl, S., Wernli, H., & Yoshimura, K. (2012). The isotopic composition of precipitation from a winter storm—A case study with the limited-area model COSMOiso. *Atmospheric Chemistry and Physics*, *12*(3), 1629–1648. https://doi.org/10.5194/acp-12-1629-2012

Rauber, R. M., Stevens, B., Ochs, H. T. III, Knight, C., Albrecht, B. A., Blyth, A. M., et al. (2007). Rain in shallow cumulus over the ocean: The RICO campaign. *Bulletin of the American Meteorological Society*, *88*(12), 1912–1928. https://doi.org/10.1175/BAMS-88-12-1912

Reisner, J., Rasmussen, R. M., & Bruintjes, R. T. (1998). Explicit forecasting of supercooled liquid water in winter storms using the MM5 mesoscale model. *Quarterly Journal of the Royal Meteorological Society*, *124*(548), 1071–1107. https://doi.org/10.1002/qj.49712454804

Riley, W. J., Still, C. J., Helliker, B. R., Ribas-Carbo, M., & Berry, J. A. (2003). O-18 composition of CO_2 and H_2O ecosystem pools and fluxes in a tallgrass prairie: Simulations and comparisons to measurements. *Global Change Biology*, *9*(11), 1567–1581. https://doi.org/10.1046/j.1365-2486.2003.00680.x

Risi, C., Bony, S., Vimeux, F., Frankenberg, C., Noone, D., & Worden, J. (2010). Understanding the Sahelian water budget through the isotopic composition of water vapor and precipitation. *Journal of Geophysical Research*, *115*, D24110. https://doi.org/10.1029/2010JD014690

Risi, C., Noone, D., Frankenberg, C., & Worden, J. (2013). Role of continental recycling in intraseasonal variations of continental moisture as deduced from model simulations and water vapor isotopic measurements. *Water Resources Research*, *49*, 4136–4156. https://doi.org/10.1002/wrcr.20312

Salamalikis, V., Argiriou, A. A., & Dotsika, E. (2016). Isotopic modeling of the sub-cloud evaporation effect in precipitation. *Science of the Total Environment*, *544*, 1059–1072. https://doi.org/10.1016/j.scitotenv.2015.11.072

Schlesinger, M. E., Oh, J.-H., & Rosenfeld, D. (1988). A parameterization of the evaporation of rainfall. *Monthly Weather Review*, *116*(10), 1887–1895. https://doi.org/10.1175/1520-0493(1988)116<1887:APOTEO>2.0.CO;2

Smith, R. B. (1992). Deuterium in North Atlantic storm tops. *Journal of the Atmospheric Sciences*, *49*(22), 2041–2057. https://doi.org/10.1175/1520-0469(1992)049<2041:DINAST>2.0.CO;2

Sodemann, H., Aemisegger, F., Pfahl, S., Bitter, M., Corsmeier, U., Feuerle, T., et al. (2017). The stable isotopic composition of water vapour above Corsica during the HyMeX SOP1 campaign: Insight into vertical mixing processes from lower-tropospheric survey flights. *Atmospheric Chemistry and Physics*, *17*(9), 6125–6151. https://doi.org/10.5194/acp-17-6125-2017

Sodemann, H., Masson-Delmotte, V., Schwierz, C., Vinther, B. M., & Wernli, H. (2008). Interannual variability of Greenland winter precipitation sources: 2. Effects of North Atlantic oscillation variability on stable isotopes in precipitation. *Journal of Geophysical Research*, *113*, D12111. https://doi.org/10.1029/2007JD009416

Soderberg, K., Good, S. P., Wang, L., & Caylor, K. (2012). Stable isotopes of water vapor in the vadose zone: A review of measurement and modeling techniques. *Vadose Zone Journal*, *11*(3). https://doi.org/10.2136/vzj2011.0165

Sommeria, G., & Deardorff, J. W. (1977). Subgrid-scale condensation in models of nonprecipitating clouds. *Journal of the Atmospheric Sciences*, *34*(2), 344–355. https://doi.org/10.1175/1520-0469(1977)034<0344:SSCIMO>2.0.CO;2

Stevens, B. (2002). Entrainment in stratocumulus-topped mixed layers. *Quarterly Journal of the Royal Meteorological Society*, *128*(586), 2663–2690. https://doi.org/10.1256/qj.01.202

Stevens, B., Moeng, C. H., Ackerman, A. S., Bretherton, C. S., Chlond, A., de Roode, S., et al. (2005). Evaluation of large-eddy simulations via observations of nocturnal marine stratocumulus. *Monthly Weather Review*, *133*(6), 1443–1462. https://doi.org/10.1175/MWR2930.1

Stevens, D. E., Ackerman, A. S., & Bretherton, C. S. (2002). Effects of domain size and numerical resolution on the simulation of shallow cumulus convection. *Journal of the Atmospheric Sciences*, *59*(23), 3285–3301. https://doi.org/10.1175/1520-0469(2002)059<3285:EODSAN>2.0.CO;2

Stewart, M. K. (1975). Stable isotope fractionation due to evaporation and isotopic-exchange of falling waterdrops—Applications to atmospheric processes and evaporation of lakes. *Journal of Geophysical Research*, *80*(9), 1133–1146. https://doi.org/10.1029/JC080i009p01133

Sullivan, P. P., McWilliams, J. C., & Moeng, C.-H. (1996). A grid nesting method for large-eddy simulation of planetary boundary-layer flows. *Boundary-Layer Meteorology*, *80*(1-2), 167–202. https://doi.org/10.1007/BF00119016

Sullivan, P. P., & Patton, E. G. (2011). The effect of mesh resolution on convective boundary layer statistics and structures generated by large-eddy simulation. *Journal of the Atmospheric Sciences*, *68*(10), 2395–2415. https://doi.org/10.1175/JAS-D-10-05010.1

Sullivan, P. P., & Patton, E. G. (2012). Corrigendum. *Journal of the Atmospheric Sciences*, *69*(3), 1155–1155. https://doi.org/10.1175/JAS-D-11-0325.1

Trenberth, K. E., Fasullo, J. T., & Kiehl, J. (2009). Earth's global energy budget. *Bulletin of the American Meteorological Society*, *90*(3), 311–324. https://doi.org/10.1175/2008BAMS2634.1

vanZanten, M. C., Stevens, B., Nuijens, L., Siebesma, A. P., Ackerman, A. S., Burnet, F., et al. (2011). Controls on precipitation and cloudiness in simulations of trade-wind cumulus as observed during RICO. *Journal of Advances in Modeling Earth Systems*, *3*, M06001. https://doi.org/10.1029/2011MS000056

Vilà-Guerau de Arellano, J., Kim, S. W., Barth, M. C., & Patton, E. G. (2005). Transport and chemical transformations influenced by shallow cumulus over land. *Atmospheric Chemistry and Physics*, *5*(12), 3219–3231. https://doi.org/10.5194/acp-5-3219-2005

Wei, Z., Lee, X., Wen, X., & Xiao, W. (2018). Evapotranspiration partitioning for three agro-ecosystems with contrasting moisture conditions: A comparison of an isotope method and a two-source model calculation. *Agricultural and Forest Meteorology*, *252*, 296–310. https://doi.org/10.1016/j.agrformet.2018.01.019

Wei, Z., Yoshimura, K., Okazaki, A., Ono, K., Kim, W., Yokoi, M., et al. (2016). Understanding the variability of water isotopologues in near-surface atmospheric moisture over a humid subtropical rice paddy in Tsukuba, Japan. *Journal of Hydrology*, *533*, 91–102. https://doi.org/10.1016/j.jhydrol.2015.11.044

Welp, L. R., Lee, X. H., Griffis, T. J., Wen, X. F., Xiao, W., Li, S. G., et al. (2012). A meta-analysis of water vapor deuterium-excess in the midlatitude atmospheric surface layer. *Global Biogeochemical Cycles*, *26*, GB3021. https://doi.org/10.1029/2011GB004246

Wen, X. F., Zhang, S. C., Sun, X. M., Yu, G. R., & Lee, X. (2010). Water vapor and precipitation isotope ratios in Beijing, China. *Journal of Geophysical Research*, *115*, D01103. https://doi.org/10.1029/2009JD012408

Wexler, A. (1976). Vapor pressure formulation for water in range 0 to 100 C. *Journal of Research of the National Bureau of Standards Section A: Physical Chemistry*, *80A*(5–6), 775–785.

Wong, T. E., Nusbaumer, J., & Noone, D. C. (2017). Evaluation of modeled land-atmosphere exchanges with a comprehensive water isotope fractionation scheme in version 4 of the Community Land Model. *Journal of Advances in Modeling Earth Systems*, *9*, 978–1001. https://doi.org/10.1002/2016MS000842

Worden, J., Noone, D., Bowman, K., Tropospheric Emission Spectrometer Science, T., & Data, c. (2007). Importance of rain evaporation and continental convection in the tropical water cycle. *Nature*, *445*(7127), 528–532. https://doi.org/10.1038/nature05508

Yamaguchi, T., & Randall, D. A. (2012). Cooling of entrained parcels in a large-eddy simulation. *Journal of the Atmospheric Sciences*, *69*(3), 1118–1136. https://doi.org/10.1175/JAS-D-11-080.1

Yoshimura, K., Frankenberg, C., Lee, J., Kanamitsu, M., Worden, J., & Rockmann, T. (2011). Comparison of an isotopic atmospheric general circulation model with new quasi-global satellite measurements of water vapor isotopologues. *Journal of Geophysical Research*, *116*, D19118. https://doi.org/10.1029/2011JD016035

Yoshimura, K., Kanamitsu, M., & Dettinger, M. (2010). Regional downscaling for stable water isotopes: A case study of an atmospheric river event. *Journal of Geophysical Research*, *115*, D18114. https://doi.org/10.1029/2010JD014032

Yoshimura, K., Kanamitsu, M., Noone, D., & Oki, T. (2008). Historical isotope simulation using reanalysis atmospheric data. *Journal of Geophysical Research*, *113*, D19108. https://doi.org/10.1029/2008JD010074

Zhao, L., Wang, L., Liu, X., Xiao, H., Ruan, Y., & Zhou, M. (2014). The patterns and implications of diurnal variations in the *d*-excess of plant water, shallow soil water and air moisture. *Hydrology and Earth System Sciences*, *18*(10), 4129–4151. https://doi.org/10.5194/hess-18-4129-2014

Erratum

In the originally published version of this article, the sequence of institutional affiliations for the first and second authors was incorrect. The order of their institutional affiliations has been corrected, and this may be considered the authoritative version of record.